NOVA SCHOOL OF SCIENCE & TECHNOLOGY

DEPARTMENT OF PHYSICS

MARIA KARIM

Bachelor of Science in Biomedical Engineering

CHARACTERIZATION OF RADIATION BEAMS FOR METROLOGY IN RADIOLOGICAL PROTECTION BY X-RAY SPECTROMETRY

MASTER IN BIOMEDICAL ENGINEERING

NOVA University Lisbon

January, 2026

NOVA SCHOOL OF SCIENCE & TECHNOLOGY

DEPARTMENT OF PHYSICS

CHARACTERIZATION OF RADIATION BEAMS FOR METROLOGY IN RADIOLOGICAL PROTECTION BY X-RAY SPECTROMETRY

MARIA KARIM

Bachelor of Science in Biomedical Engineering

Adviser: Andreas Kling
Principal Researcher, Instituto Superior Técnico, University of Lisbon

Co-adviser: João Duarte Neves Cruz
Associate Professor, NOVA University Lisbon

MASTER IN BIOMEDICAL ENGINEERING

NOVA University Lisbon
January, 2026

Characterization of radiation beams for metrology in Radiological Protection by X-ray spectrometry

This document was created with the (pdf/Xe/Lua)LaTeX processor and the NOVAthesis template (v7.3.1) [1].

My children ! Helal, Atiya, Zualal and Ruwaida. I did it, and may each of you go further and rise higher than I ever could.

Acknowledgements

I would like to express my deepest gratitude to Professor Andreas Kling for his guidance, support, and dedication throughout this work. His expertise and patience were fundamental in helping me develop a strong interest in the field of radiation and radiology, and his continuous encouragement greatly contributed to the progress of this thesis.

I also wish to thank Professor Ana Fernandes for her consistent motivation and for facilitating access to the LMRI laboratory whenever required. I am similarly grateful to the LMRI laboratory staff for their constant friendliness and readiness to assist during the experimental procedures.

My sincere appreciation extends to Professor João Cruz, my co-supervisor, for his valuable guidance and availability whenever support was needed, as well as to the Department of Physics of NOVA FCT for their support throughout my academic journey.

I would like to express my heartfelt thanks to my husband, Shamsuddin Ahmadzai, for his unwavering support, encouragement, and patience throughout this demanding academic journey. His strength and understanding made it possible for me to focus on my studies during periods of significant pressure and responsibility.

A very special acknowledgment goes to my four children Helal, Atiya, Ruwaida, and Ahmad Zulal. Their patience, love, and resilience gave me the motivation to continue, even during the most challenging stages of this work. They endured my long hours of absence and countless days when I was fully committed to academic responsibilities. I am deeply grateful for their understanding and for the joy they bring into my life every day. This achievement belongs to them as much as it belongs to me, and I hope it serves as an example of perseverance and dedication for their future.

Finally, I would like to thank everyone who contributed, directly or indirectly, to the completion of this work.

Abstract

Ensuring accurate metrological verification of ionizing radiation monitoring equipment is a crucial task in the area of radiological protection of exposed workers and patients subjected to ionizing radiation. This work aims to enhance the metrological verification of X-ray detection equipment at the Portuguese Metrology Laboratory of Ionizing Radiation (Laboratório de Metrologia de Radiações Ionizantes, LMRI), located at the Technological and Nuclear Campus of Instituto Superior Técnico, University of Lisbon. The study explores the application of X-ray spectrometry employing cadmium telluride detectors to perform systematic studies on the properties of the X-ray beams available at LMRI allowing for the extension of calibration conditions beyond those currently available. For this purpose, the energy spectra of the beams were measured as a function of the distance from the source, tube current and acceleration voltage. Monte Carlo methods were employed to assess the detector's response to monoenergetic radiation and to build a response function matrix for reconstructing continuous X-ray spectra from the measured data using deconvolution algorithms. As an additional asset, methods for determining the spectral endpoint were implemented based on a machine learning algorithm offering an alternative approach to precisely determine the acceleration potential of the X-ray tube.

Keywords: X-ray spectrometry, Metrology, Radiological protection, Radiology Monte Carlo simulations, Deconvolution algorithm, X-ray detector response, Calibration conditions.

Declaration of Originality The research work described in this dissertation was carried out in accordance with the norms established in the ethics code of Universidade Nova de Lisboa. The work described and the material presented in this dissertation, with the exceptions clearly indicated, constitute original work carried out by Maria Karim.

Resumo

O controlo metrológico legal dos instrumentos de medição de radiações ionizantes assegura a qualidade metrológica de medidas importantes para a proteção radiológica de trabalhadores expostos e pacientes sujeitos a exposição médica. Este trabalho destina-se ao aperfeiçoamento das operações de verificação metrológica, asseguradas a nível nacional pelo Laboratório de Metrologia de Radiações Ionizantes (LMRI) do Instituto Superior Técnico, Universidade de Lisboa. Neste trabalho, a espectrometria de radiação X com recurso a um detetor de telureto de Cádmio foi implementada e explorada para caracterização dos feixes de radiação de referência do LMRI, permitindo ampliar as condições de utilização dos feixes em relação à prática atual. A matriz de resposta do detetor, construída com base em simulações do transporte de radiação pelo método de Monte Carlo e validada por medições com fontes monoenergéticas, foi utilizada para calcular a distribuição energética dos fotões a partir do sinal medido (desconvolução). A distribuição energética de feixes de raios X do LMRI foi medida em diversas condições de exposição quanto à filtração do feixe, distância em relação à fonte, intensidade da corrente no filamento e potencial de aceleração na ampola. Adicionalmente, foi desenvolvida uma nova metodologia para a determinação do potencial de aceleração da ampola de raios X com base na aplicação de algoritmos de machine learning dispensando o processo de desconvolução.

Palavras-chave: Espectrometria de raios-X, Metrologia, proteção radiológica, radiologia, simulação Monte-Carlo, algoritmos de desconvolução, resposta de detetores de raios-X, condições de calibração.

Declaração de Originalidade O trabalho de investigação descrito nesta dissertação foi realizado de acordo com as normas estabelecidas no código de ética da Universidade Nova de Lisboa. O trabalho descrito e o material apresentado nesta dissertação, com as exceções claramente indicadas, constituem trabalho original realizado por Maria Karim.

Contents

List of Figures

List of Tables

Acronyms

ARPANSA Australian Radiation Protection and Nuclear Safety Agency *(p. 15)*

CCT Charge Collection Tailing *(pp. 10, 23)*
CdTe cadmium telluride *(p. 2)*
CTE Charge Transport Efficiency *(p. 10)*

DppMCA Amptek Digital Pulse Processor Multi-Channel Analyzer *(p. 18)*

EURAMET European Association of National Metrology Institutes *(p. 17)*

FWHM Full Width at Half Maximum *(pp. 10, 11)*

GRAVEL GRouped AVERage unfolding algorithm *(pp. 13, 18)*

HVL Half-Value Layer *(pp. 6, 15)*

IAEA International Atomic Energy Agency *(p. 2)*
ICC Incomplete Charge Collection *(pp. 10, 23)*
ICRU International Commission on Radiation Units and Measurements *(p. 17)*
IPQ Portuguese Institute of Quality *(p. 2)*
ISO International Organization for Standardization *(p. 1)*

LMRI Ionizing Radiation Metrology Laboratory *(pp. 1–3, 18, 19)*
LPSR Laboratory of Radiological Protection and Safety *(p. 2)*

MAE Mean Absolute Error *(p. 31)*
MAXED Maximum Entropy Deconvolution *(pp. 13, 18)*
MCA Multi-Channel Analyzer *(p. 18)*

PHITS Particle and Heavy Ion Transport code System *(p. 18)*

1

Introduction

1.1 Context and Motivation

Radiation protection aims to minimize health risks associated with exposure to ionizing radiation. Accurate measurements of X-ray radiation are therefore essential to ensure compliance with international safety standards and to guarantee the traceability of calibration results used in radiation protection. In this context, radiation protection calibration laboratories rely on well-defined reference radiation fields to calibrate and verify radiation measuring instruments, thereby ensuring consistency and comparability of measurements across laboratories [2].

Radiation detectors measure physical quantities related to energy deposition in matter, such as absorbed dose or air kerma, expressed in units of gray (Gy). While these quantities provide a physical description of radiation interactions, they do not directly represent the biological effect of radiation exposure. For radiation protection purposes, absorbed dose must therefore be converted into operational dose equivalent quantities, expressed in sievert (Sv), using energy- and geometry-dependent conversion coefficients defined by international recommendations [3, 4]. The validity of these conversion coefficients depends critically on the photon energy spectrum of the radiation field.

Accurate determination of operational dose quantities consequently requires well characterized radiation fields, since variations in the X-ray energy spectrum and irradiation geometry directly affect detector response and dose conversion factors. Standard calibration procedures at the Ionizing Radiation Metrology Laboratory (LMRI) are performed in compliance with International Organization for Standardization (ISO) 4037 and are primarily based on air-kerma measurements and nominal X-ray tube settings. However, this approach provides limited information on the actual spectral distribution of the radiation field and does not allow independent verification of the X-ray tube acceleration potential [2]. As a result, no spectrometric procedure was being implemented at the LMRI to support verification activities under varying irradiation conditions, such as changes in source detector distance or tube current.

X-ray spectrometry, combined with detector response modelling and spectrum unfolding

techniques, provides a powerful tool for characterizing X-ray beams beyond integral dosimetric quantities. In particular, spectrometric methods enable reconstruction of the photon energy distribution and allow independent estimation of the X-ray tube acceleration potential through endpoint energy analysis. Although such approaches have been demonstrated as effective tools for beam characterization and tube voltage verification in radiation protection metrology [5, 6], their systematic implementation was lacking, motivating the present work.

1.2 Laboratory of Ionizing Radiation Metrology (LMRI)

The Laboratory of Radiological Protection and Safety (LPSR) at the Nuclear Technology Campus of Instituto Superior Técnico conducts activities in ionizing radiation metrology, individual and environmental dosimetry, and biological dosimetry [7].

Within the LPSR, the LMRI has been designated by the Portuguese Institute of Quality (IPQ) as the national reference laboratory for ionizing radiation and is accredited as a Metrological Verification Body for radiation measuring instruments. In addition, the LMRI participates in the International Atomic Energy Agency (IAEA)/WHO network of Secondary Standards Dosimetry Laboratories [8, 9].

The LMRI provides reference radiation fields for calibration and verification purposes, including ^{137}Cs and ^{60}Co gamma-ray sources, as well as X-ray beams generated in accordance with ISO 4037 specifications. At present, calibration services are mainly focused on air kerma, in line with standard calibration practice defined in ISO 4037 [2]. The introduction of X-ray spectrometry for beam characterization supports enhanced traceability and reliability of radiation protection calibrations performed within the LPSR.

1.3 Objectives

This study intends to improve X-ray radiation protection metrology through the spectrometric characterization of LMRI's X-ray beams. The intended tasks are:

- Measure and analyse X-ray energy spectra using a cadmium telluride (CdTe) semiconductor detector under different irradiation conditions, including variations in source detector distance and tube current.
- Determine the acceleration potential of the X-ray tube by analysing the endpoint energy of the X-ray spectrum using linear extrapolation and tangent-based methods.
- Reconstruct continuous X-ray spectra from measured detector data using Monte Carlo–based detector response functions and spectrum unfolding algorithms, including MAXED and GRAVEL.
- Complement existing air-kerma-based calibration procedures by introducing a spectrometric approach to support beam-quality and tube-voltage verification.

2

THEORETICAL CONCEPTS

2.1 Fundamentals of Ionizing Radiation

Ionizing radiation is defined by its ability to excite and ionize atoms of matter. Since the energy required to remove a valence electron is of the order of a few electron volts (4–25 eV), radiation must carry energies above this range to be classified as ionizing [10, 11]. This property is central to radiation protection, as ionization processes govern energy deposition in matter and the response of radiation detectors [4]. In this work, only X-ray photons are considered, as they are directly relevant to calibration and metrological verification at the LMRI [2].

2.1.1 Interaction of X-rays with matter

X-rays interact with matter through several fundamental mechanisms, including coherent (Rayleigh) scattering, Compton scattering, photoelectric absorption, pair production, and photodisintegration [10, 11]. The relative importance of each interaction depends primarily on the photon energy and the atomic number (Z) of the material.

In the X-ray energy range relevant to radiation protection and spectrometric measurements (approximately 10–150 keV), the dominant interaction mechanisms are photoelectric absorption and Compton scattering [10, 12]. Photoelectric absorption is strongly dependent on the atomic number of the absorbing material and dominates at lower photon energies, playing a major role in detector efficiency and beam attenuation, particularly for high-Z materials such as CdTe [13, 14]. Compton scattering becomes increasingly significant at intermediate energies and contributes to spectral broadening and background in detector measurements [11]. Pair production and photodisintegration occur only at much higher photon energies and are therefore not relevant in this work [10].

2.1.2 Attenuation and Absorption of X-rays

When an X-ray beam propagates through matter, its intensity decreases due to photon interactions with the material. This reduction, known as attenuation, results from a combination of absorption and scattering processes [4, 10]. For a narrow, monoenergetic

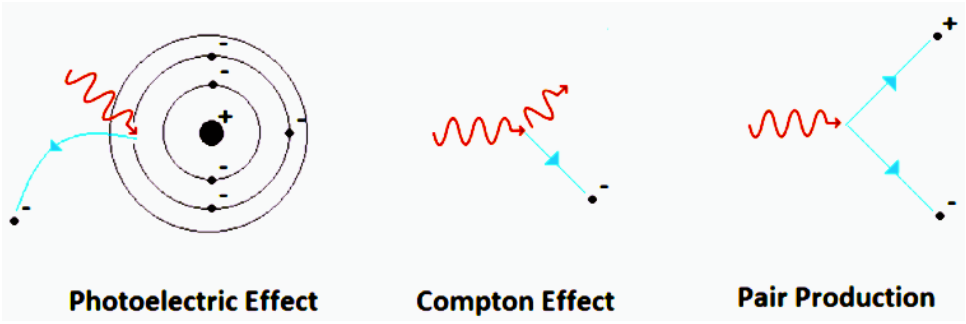

Figure 2.1: Photon interactions with matter: photoelectric effect, Compton effect, and pair production. Adapted from [15].

X-ray beam, the attenuation can be described by the Beer–Lambert law:

$$I = I_0 e^{-\mu x}, \tag{2.1}$$

where I_0 and I are the incident and transmitted intensities, respectively, after passing through a material thickness x, and μ is the linear attenuation coefficient. The coefficient μ depends on the photon energy and the atomic composition of the material [10, 13].

2.2 X-ray Generation and Properties

2.2.1 Bremsstrahlung and Characteristic Radiation

In conventional X-ray tubes, X-rays are generated by accelerating electrons from a heated cathode toward a metal target (anode) under vacuum. X-ray production occurs through two primary mechanisms: Bremsstrahlung radiation and characteristic radiation. Bremsstrahlung radiation is produced when high-speed electrons are decelerated in the electric field of atomic nuclei in the target material, generating a continuous X-ray spectrum whose maximum photon energy (end-point energy) is determined by the applied tube voltage. The intensity of this radiation increases with both tube voltage and the atomic number (Z) of the target material. Characteristic radiation arises when an incident electron ejects an inner-shell electron from the target atom, and the subsequent atomic relaxation produces photons with discrete energies characteristic of the anode material [11, 12].

2.2.2 Properties of X-rays

X-ray beams generated in conventional tubes are polyenergetic, consisting of a continuous Bremsstrahlung spectrum superimposed with characteristic emission lines. The photon energy E is related to the wavelength λ by

$$E = \frac{hc}{\lambda}, \tag{2.2}$$

where h is Planck's constant and c is the speed of light.

The spectral distribution and penetrating power of X-rays are primarily governed by the tube voltage and filtration. Increasing the tube voltage raises the end-point energy and

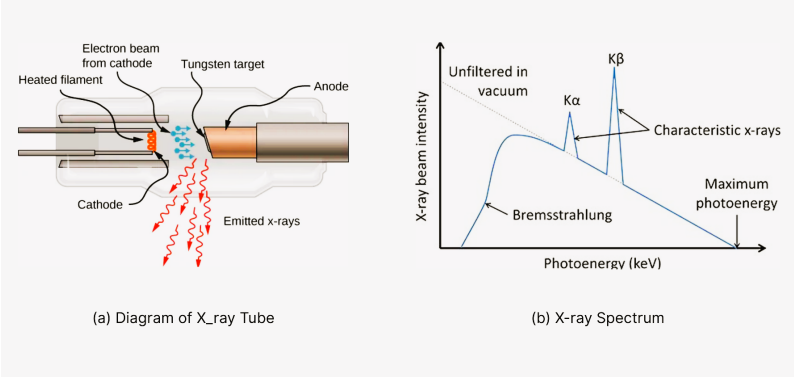

Figure 2.2: Conventional X-ray tube and emitted spectrum: (a) tube schematic showing the cathode, anode, and electron acceleration toward the tungsten target; (b) corresponding X-ray spectrum with Bremsstrahlung continuum, characteristic Kα and Kβ lines, and the maximum photon energy, adapted from [15].

shifts the spectrum toward higher energies, producing a harder beam, while filtration preferentially removes low-energy photons and modifies the beam quality relevant for radiation protection metrology [2, 10].

2.2.3 X-ray Tube Components and Operation

An X-ray tube is a vacuum device designed to generate X-rays by accelerating electrons toward a metal target under a high electric potential [12]. Its essential components include the cathode, anode, vacuum envelope, high-voltage power supply, and cooling system.

- **Cathode:** The cathode acts as the electron source and typically consists of a heated tungsten filament that emits electrons by thermionic emission. The emitted electron current directly controls the intensity of the produced X-ray beam [11, 12].
- **Anode:** The anode serves as the target for the accelerated electrons and is commonly made of tungsten due to its high atomic number and high melting point. Electron deceleration in the anode produces X-rays via Bremsstrahlung and characteristic emission [11].
- **Vacuum envelope and window:** The cathode–anode assembly is enclosed in a vacuum envelope to prevent electron interactions with air. X-rays exit the tube through a thin window, typically made of beryllium, which minimizes photon attenuation [12].
- **High-voltage supply and cooling:** A high-voltage power supply accelerates electrons from the cathode to the anode and determines the maximum photon energy of the emitted spectrum. Since most electron energy is converted into heat, active cooling is required to maintain stable tube operation [11].

The stability and control of tube voltage and current are critical for reproducible X-ray spectra and are therefore of primary importance in radiation protection metrology [2].

2.2.4 Influence of Tube Voltage and Filtration on the X-ray Spectrum

The tube voltage (kVp) is a key parameter governing the X-ray energy spectrum. Increasing the applied voltage shifts the Bremsstrahlung continuum toward higher energies and increases the maximum photon energy, known as the end-point energy [11, 12]. Discrete characteristic emission lines appear only when the tube voltage exceeds the binding energies of the inner atomic shells of the anode material [11]. Accurate control of the tube voltage is therefore essential for defining the spectral shape of the X-ray beam, and the determination of the tube acceleration potential from the spectral end-point represents a metrological problem addressed by standardized spectrometric approaches such as ISO 16526 [16].

Filtration refers to the placement of absorbing materials, such as aluminum or copper, in the X-ray beam to modify its spectral composition [10]. These materials preferentially attenuate low-energy photons, resulting in an increase of the mean photon energy of the beam (beam hardening) [11]. Filtration therefore plays a key role in defining beam quality and ensuring stable and reproducible X-ray spectra for radiation protection metrology and calibration procedures [2].

2.2.5 Beam Quality Parameters

Beam quality describes the penetrating power of an X-ray beam and is primarily determined by its spectral composition, which depends on tube voltage and filtration [2, 10]. A commonly used beam quality parameter is the Half-Value Layer (HVL), defined as the thickness of a specified material, typically aluminum, required to reduce the beam intensity by 50% [4, 10]. HVL provides an integral measure of beam hardness and is widely used in radiation protection calibration and verification procedures [17].

2.3 Dosimetric Quantities and Units

Dosimetric quantities are used to describe ionizing radiation in terms of energy deposition and radiation field strength. While several quantities exist, radiation metrology primarily relies on physical quantities that can be measured accurately and reproduced under reference conditions [4, 10]. The absorbed dose D represents the mean energy deposited by ionizing radiation per unit mass of a material and is expressed in gray (Gy). To account for differences in biological effectiveness between radiation types, the absorbed dose can be converted into equivalent dose H using a radiation weighting factor w_R:

$$H = D \cdot w_R. \tag{2.3}$$

For X-rays, $w_R = 1$, such that absorbed dose and equivalent dose are numerically identical when expressed in Gy and Sv, respectively [3, 10]. The effective dose E further combines equivalent doses to different organs using tissue weighting factors w_T,

$$E = \sum_T w_T H_T, \tag{2.4}$$

and is mainly used for radiation protection and regulatory purposes. Because it depends on human anatomy and irradiation geometry, the effective dose is not directly measurable [3, 4]. In X-ray radiation protection metrology, the reference quantity most commonly used is air kerma, defined as the kinetic energy transferred from photons to secondary electrons per unit mass of air. Air kerma, expressed in gray (Gy), provides a practical and traceable basis for the characterization and calibration of X-ray radiation fields [2, 4].

2.3.1 Operational Quantities in Radiation Protection

Protection quantities such as effective dose cannot be measured directly, as they are defined for idealized human geometries and tissue sensitivities [3]. For practical radiation monitoring and calibration purposes, operational quantities are therefore introduced. These quantities are defined so that they can be measured using calibrated instruments and provide conservative estimates of protection quantities under reference conditions [2, 17]. In external photon radiation fields, the most relevant operational quantity for area monitoring is the ambient dose equivalent, $H^*(d)$. It is defined as the dose equivalent at a depth d in a standardized phantom, commonly $d = 10$ mm for X- and gamma radiation, in an aligned and expanded radiation field. The quantity $H^*(10)$ is widely used to characterize radiation fields and to verify compliance with reference calibration conditions [18].

For individual monitoring, the personal dose equivalent, $H_p(d)$, is defined as the dose equivalent in soft tissue at a depth d below a specified point on the body. In whole-body dosimetry, $H_p(10)$ is commonly used. Both $H^*(10)$ and $H_p(10)$ are expressed in sievert (Sv) and are derived from measurable physical quantities using energy- and geometry-dependent conversion coefficients [18].

In radiation protection metrology, these operational quantities are realized through calibration procedures based on reference radiation fields, which are typically characterized in terms of air kerma. Accurate knowledge of the X-ray beam spectrum is therefore essential for establishing reliable conversion coefficients and ensuring traceability of operational dose measurements [2, 17].

2.3.2 Conversion Factors for Radiation Protection Dosimetry

In radiation protection metrology, conversion factors are used to relate measurable physical quantities to operational dose quantities. In the case of photon radiation, these factors are applied to convert air kerma into quantities such as ambient and personal dose equivalents. The conversion factors depend on the photon energy and irradiation geometry and are derived from radiation transport calculations [3, 4]. Because conversion coefficients are energy dependent, accurate knowledge of the X-ray beam spectrum is essential for reliable dose estimation. Spectral variations directly influence the calculated operational quantities, highlighting the importance of spectrometric beam characterization in radiation protection calibration procedures [2, 5].

2.4 X-ray Spectrometry in Radiation Metrology

X-ray spectrometry is used in radiation metrology to determine the energy distribution of photons emitted by X-ray sources. While air kerma measurements provide information on the total radiation output, they do not describe the energy-dependent structure of the X-ray beam. Spectrometric measurements therefore offer complementary information that is required for beam quality characterization and verification of X-ray tube operating conditions [2, 5, 19].

2.4.1 Semiconductor Detectors for X-ray Spectrometry

Semiconductor detectors are widely used in X-ray spectrometry because they enable direct, energy-resolved measurements of incident photons. When an X-ray photon interacts within a semiconductor material, its energy is converted into a number of electron–hole pairs that is proportional to the deposited energy. By collecting this charge under an applied electric field, the photon energy can be reconstructed with good resolution [11, 20].

Compared to gas-filled detectors, semiconductor detectors offer superior energy resolution and compact detector geometry, making them suitable for spectrometric measurements in the diagnostic and radiation metrology energy range. Their stable response and compatibility with digital signal processing systems allow accurate characterization of X-ray spectra in laboratory environments [11, 21].

2.4.1.1 CdTe Detectors

Cadmium telluride (CdTe) detectors are well suited for X-ray spectrometry in radiation metrology due to their high photon detection efficiency in the diagnostic energy range. The high atomic numbers and density of CdTe provide a much higher absorption probability than silicon detectors, allowing efficient detection of X-ray photons up to and above 100 keV with compact detector volumes [14, 20].

In addition, the wide band gap of CdTe enables stable operation at room temperature, eliminating the need for cryogenic cooling and simplifying laboratory measurements. For these reasons, CdTe detectors are commonly used for X-ray beam characterization and calibration applications [19, 21]. However, their spectral response is non-ideal and must be modeled for accurate quantitative spectrometric analysis [5].

2.4.1.2 Non-ideal response effects in CdTe detectors

Although CdTe detectors provide high detection efficiency for X-ray spectrometry, their energy response is affected by several non-ideal effects related to charge transport and photon interactions within the detector material. These effects distort the measured

spectral shape and must be understood and modeled to achieve accurate quantitative spectrometric results [20–23].

2.4.1.3 Problem of Charge Trapping and Tailing

When X-ray photons interact with the CdTe crystal, electron–hole pairs are generated and drift toward the electrodes under the applied electric field. Due to the relatively low mobility and shorter lifetime of holes, a fraction of these charge carriers becomes trapped within the crystal lattice before reaching the electrodes. As a consequence, the total collected charge is reduced. This incomplete charge collection leads to a systematic underestimation of the deposited energy and results in a characteristic low-energy tail on the photopeak [20, 21].

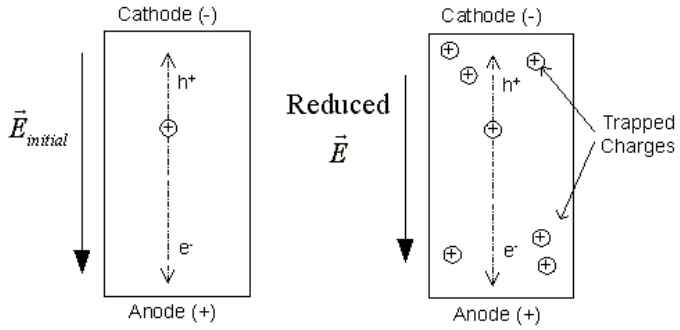

Figure 2.3: Illustrative diagram of charge trapping and low-energy tailing in a CdTe detector. Adapted from [23].

2.4.1.4 Escape Peaks in CdTe Detectors

When a photon is fully absorbed in CdTe via a K-shell photoelectric interaction, the subsequent atomic relaxation may involve the emission of a characteristic K X-ray from cadmium or tellurium. If this fluorescent photon escapes the sensitive detector volume instead of being reabsorbed, the recorded energy is reduced by the corresponding K-line energy. This process produces escape peaks at energies given by

$$E_{\text{esc}} \approx E_{\gamma} - E^{\text{Cd/Te}}_{K\alpha,K\beta}.$$

For CdTe, the characteristic K-line energies are approximately 23.17 keV and 26.10 keV for Cd K_{α} and K_{β}, and 27.47 keV and 31.00 keV for Te K_{α} and K_{β}, respectively [21, 22]. For the ^{241}Am 59.54 keV line, escape peaks are therefore expected in the range from approximately 28 to 36 keV, consistent with the satellite structures observed around the main photopeak [21, 22]. The probability of escape events increases for interactions occurring close to the detector surface and depends on the photon energy and detector thickness [21]. These escape peaks represent a characteristic signature of CdTe detectors and must be accounted for in spectrometric analysis [21, 22].

2.4.2 Carrier Trapping Effect (CTE) Model

The Carrier Trapping Effect (CTE) describes charge losses occurring during the drift of charge carriers toward the electrodes due to trapping centers in the CdTe crystal [20, 21]. The fraction of charge successfully collected, referred to as the charge collection efficiency (CCE), can be described using a modified Hecht equation [14, 21]:

$$\mathrm{CCE}(z) = \frac{K_e}{d}\left[\lambda_h\left(1 - e^{-\frac{z}{\lambda_h}}\right) + \lambda_e\left(1 - e^{-\frac{d-z}{\lambda_e}}\right)\right], \qquad K_e = \frac{d/\lambda_e}{1 - e^{-d/\lambda_e}} \tag{2.5}$$

where d is the detector thickness, λ_e and λ_h are the mean drift lengths of electrons and holes, respectively, and z is the interaction depth within the sensor. The normalization factor K_e ensures correct alignment of the full-energy peak [14, 21]. Although the model assumes a uniform electric field, small depth-dependent variations are typically included to improve agreement with experimental data [21, 22].

2.4.3 Incomplete Charge Collection (ICC) Model

In addition to bulk trapping, incomplete charge collection occurs in near-surface regions beneath the detector electrodes, commonly referred to as dead layers. Charge generated in these regions contributes only partially to the measured signal [21, 22]. This effect is described by the carrier collection probability (CCP), expressed as [22, 23]

$$\mathrm{CCP} = 1 - (1 - RC)\, e^{-z v_s / D}, \tag{2.6}$$

where RC is the reflectivity, v_s is the saturation velocity, D is the effective diffusion coefficient, and z is the interaction depth. The ICC effect is most relevant at lower photon energies, where interactions occur predominantly near the detector surface [21]. Combined with CTE, it provides a complete description of CdTe charge transport behavior [20, 22].

2.4.4 Detector Energy Resolution

Even after correcting for charge transport effects, the measured energy spectrum is broadened due to statistical fluctuations in electron–hole pair generation and electronic noise in the readout system. This intrinsic energy resolution is typically modeled by Gaussian broadening, with the Full Width at Half Maximum (FWHM) increasing with photon energy [11, 21]. In detector response simulations, the resolution function is applied after CTE and ICC corrections to reproduce realistic peak widths and asymmetries [5, 21].

2.4.5 Analytical Model (CCT Integration)

By combining the Charge Transport Efficiency (CTE) and the Incomplete Charge Collection (ICC) models, a Charge Collection Tailing (CCT) description of the CdTe detector response is obtained [5, 22]. This model corrects the initial photon energy E_i for charge losses

occurring both in the bulk of the detector and in near-surface regions, according to

$$E_{\mathrm{CCT}} = \mathrm{CTE} \cdot \mathrm{ICC} \cdot E_i. \tag{2.7}$$

To account for the finite detector energy resolution, the corrected energy E_{CCT} is subsequently broadened using a Gaussian response function, yielding the reconstructed energy

$$E_{\mathrm{rec}} = E_{\mathrm{CCT}} + b \cdot \sigma(E_{\mathrm{CCT}}), \tag{2.8}$$

where b is a random variable drawn from a normal distribution and $\sigma(E_{\mathrm{CCT}})$ is derived from the detector FWHM at the corresponding energy. This integrated analytical model enables simulated spectra to reproduce the measured CdTe detector response, accounting simultaneously for charge transport effects and energy resolution broadening [5].

2.4.5.1 Analysis of ^{241}Am Spectrum

The ^{241}Am source provides a well-defined reference for assessing the spectrometric response of the CdTe detector, as illustrated in Fig. 2.4. The spectrum is dominated by the 59.54 keV photopeak, accompanied by several lower-energy features. The measured distribution exhibits a pronounced low-energy tail, mainly attributed to incomplete charge collection caused by hole trapping in the CdTe crystal [21–23]. In addition, multiple escape peaks are observed, originating from characteristic fluorescence of Cd and Te following photoelectric interactions. The asymmetric shape of the 59.54 keV peak reflects the depth-dependent charge transport properties of CdTe detectors and the associated energy-loss mechanisms [24].

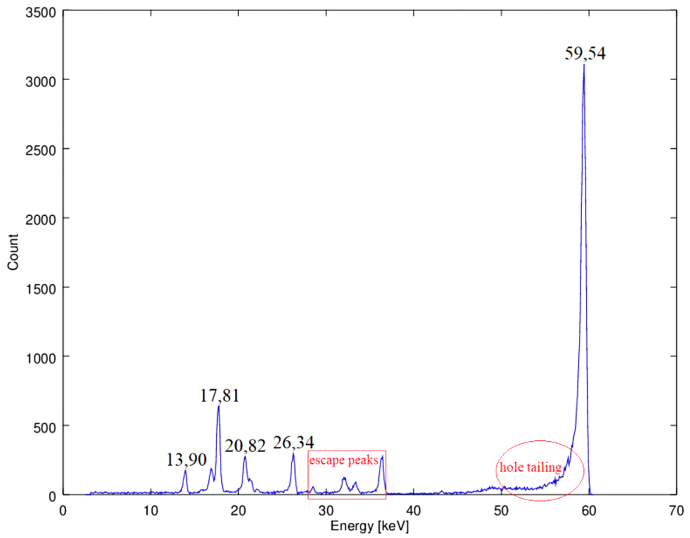

Figure 2.4: Measured ^{241}Am spectrum showing the main photopeak, escape peaks, and low-energy tailing due to incomplete charge collection. *Adapted from* [24].

2.5 Monte Carlo Simulations in Radiation Metrology

2.5.1 Overview of the Monte Carlo Method

The Monte Carlo method is a statistical approach based on random sampling to model physical processes that are analytically intractable due to their complexity. In radiation metrology, it is widely used to simulate the transport and interaction of ionizing radiation with matter, providing a detailed description of energy deposition processes under well-defined irradiation conditions.

2.5.2 Application in Radiation Detector Response Studies

Monte Carlo simulations are extensively employed to model the transport of photons and secondary particles in detector materials [25]. In these simulations, particles are generated with randomized initial parameters such as position, direction, and energy, and their trajectories are followed according to interaction probabilities derived from fundamental cross sections [21]. Repeating this process for a large number of particles yields a statistically robust representation of the energy deposition in the detector.

In the context of X-ray spectrometry, Monte Carlo methods are particularly important for calculating detector response functions, defined as the pulse-height spectra produced by monoenergetic photons [5]. Detector-specific effects, including energy resolution broadening and charge transport losses, can be incorporated using analytical models such as the CCT framework described previously. The resulting response matrices form a key input for spectrum unfolding algorithms, enabling the reconstruction of the true photon fluence spectrum from measured data.

2.5.3 Control and Stability of X-ray Tube Acceleration Potential

In X-ray spectrometric measurements, the control and stability of the tube acceleration potential are critical factors that directly influence the shape of the emitted spectrum. Variations in tube voltage affect the maximum photon energy (end-point energy) and the overall spectral distribution, leading to systematic distortions in measured pulse-height spectra. Ensuring stable and reproducible tube potential is therefore essential for accurate spectral characterization, response matrix generation, and reliable spectrum unfolding in radiation metrology applications [6, 16].

2.6 Spectrum Unfolding Methods

Accurate knowledge of the photon fluence spectrum is essential for the metrological characterization of reference radiation fields and for the calibration of dosimetric instruments [2]. Spectra measured with semiconductor detectors such as CdTe do not directly represent the true incident photon field due to detector-specific effects, including escape peaks, incomplete charge collection, and electronic noise [20, 21]. To correct for these distortions, an inverse computational procedure known as *unfolding* is applied.

This process reconstructs the most probable photon energy distribution by combining the measured spectrum with a detector response matrix and appropriate numerical algorithms [5].

2.6.1 Mathematical Basis

The unfolding problem can be formulated as a linear system:

$$\mathbf{y} = \mathbf{R} \cdot \mathbf{\Phi} + \boldsymbol{\varepsilon}, \tag{2.9}$$

where $\mathbf{y}$ represents the measured pulse-height spectrum, $\mathbf{R}$ is the detector response matrix, $\mathbf{\Phi}$ is the unknown photon fluence spectrum, and $\boldsymbol{\varepsilon}$ accounts for statistical and systematic noise [26, 27]. This problem is ill-posed, as small fluctuations in the measured data may lead to large variations in the solution. Regularized and iterative methods are therefore required to obtain stable and physically meaningful results [28].

2.6.2 Unfolding Algorithms

Among the available unfolding techniques, two algorithms are widely used in radiation metrology. The Maximum Entropy Deconvolution (MAXED) method reconstructs the smoothest spectrum consistent with the measured data by maximizing entropy under the constraint imposed by Eq. 2.9 [26]. The GRouped AVERage unfolding algorithm (GRAVEL) employs an iterative least-squares approach with intrinsic regularization, progressively updating the spectrum estimate to minimize residuals between calculated and measured responses [27, 28]. Both methods rely on accurate detector response matrices and are well suited for reconstructing continuous X-ray spectra [5].

2.6.3 Detector Response Matrices

The detector response matrix $\mathbf{R}$ describes the probability that photons of a given energy contribute to specific channels of the measured spectrum. In practice, response matrices are obtained from Monte Carlo simulations and must incorporate the detector geometry, dead layers, charge transport effects described by the CCT model, and energy resolution broadening [5, 22]. Proper conditioning of the response matrix is essential to ensure numerical stability during the unfolding process [27].

2.6.4 Uncertainty Considerations and Validation

Unfolded spectra are subject to uncertainties arising from counting statistics, detector modeling assumptions, and algorithmic regularization [26, 27]. Quantifying and propagating these uncertainties is essential to maintain metrological traceability [17]. Validation of unfolded results is typically performed through comparison with theoretical spectra, independent Monte Carlo simulations, and integral beam parameters such as the mean photon energy or the (HVL) [2, 5].

3

STATE OF THE ART

3.1 Scope of the Chapter

This chapter reviews international standards and best laboratory practices for the realisation of reference X-ray radiation fields in radiation protection metrology. It then discusses the methodological issues associated with standardised approaches based on integral beam parameters and motivates the use of X-ray spectrometry. Finally, the chapter identifies existing gaps in current practice and outlines how the methodology developed in this thesis addresses them.

3.2 Reference Radiation Fields in Radiation Protection Laboratories

Radiation protection calibration laboratories rely on physically realisable and reproducible photon reference fields to ensure traceable calibration of dosimeters and radiation measuring instruments. For photon radiation, such fields are typically produced using filtered X-ray beams from X-ray tubes or discrete gamma-ray emissions from radionuclide sources, providing stable irradiation conditions for routine calibration work [2, 17]. The designation and use of these reference photon fields are governed by the ISO 4037 series. ISO 4037-1 defines nominal reference radiation qualities, ISO 4037-2 specifies procedures for establishing and verifying matched fields, and ISO 4037-3 provides conversion coefficients linking physical quantities to operational dose quantities. Together, these standards ensure comparability and traceability of calibration results across radiation protection laboratories [2, 17, 18].

3.3 Classification of X-ray Radiation Fields for Calibration

In radiation protection metrology, X-ray radiation fields are classified to provide well-defined and reproducible reference conditions for the calibration of dosimeters and radiation measuring instruments. This classification is based on measurable beam parameters rather than detector physics or detailed radiation interaction models.

According to the ISO 4037 series, reference X-ray radiation fields are defined by standardised combinations of tube voltage, filtration, and beam quality indicators such as the HVL, which are assigned specific radiation quality designations for calibration purposes [2, 17]. In the diagnostic and radiation protection energy ranges, reference fields are typically generated using tungsten anode X-ray tubes with selected filtration materials, most commonly aluminium, copper, or tin [2]. Filtration thickness is adjusted so that the resulting HVL and beam quality parameters match the nominal values specified by the standard [2, 17]. Different combinations of tube voltage and filtration may lead to similar HVL values; however, only radiation fields fulfilling the ISO-defined criteria are accepted as reference qualities [17, 29].

3.4 Challenges of ISO Radiation Qualities for Spectral Analysis

The ISO 4037 classification provides a practical and traceable framework for the calibration of radiation protection instruments [2, 17]. However, because reference radiation qualities are defined using integral beam parameters, this approach does not uniquely define the underlying photon fluence spectrum of the radiation field. In practice, different X-ray spectra may satisfy the same ISO radiation quality designation while exhibiting noticeable differences in spectral shape, particularly in the low- and intermediate-energy regions. These differences arise from variations in tube design, inherent filtration, added filtration, anode angle, and operating conditions, and may lead to deviations in energy-dependent quantities despite identical HVL values [5]. This limitation is critical for energy-dependent applications (e.g., conversion coefficients and Monte Carlo validation), where integral beam parameters alone can mask relevant spectral differences and introduce systematic uncertainties. Experimental evidence from radiation metrology laboratories supports this limitation. Studies reported by Australian Radiation Protection and Nuclear Safety Agency (ARPANSA) demonstrate that multiple combinations of inherent and added filtration can satisfy the same HVL-based criteria, particularly for heavily filtered beam qualities [30]. As a result, radiation fields meeting the same ISO designation may differ in photon fluence spectrum while remaining indistinguishable when characterised solely by integral quantities such as air kerma and HVL. This practical variability provides a clear justification for the use of X-ray spectrometry and spectrum unfolding as complementary tools in radiation protection metrology, enabling direct reconstruction of the photon fluence spectrum and a more complete characterisation of ISO reference radiation qualities [5].

3.5 X-ray Spectrometry and Spectrum Unfolding in Radiation Metrology

To overcome the challenges of radiation field characterisation based solely on integral beam parameters, X-ray spectrometry has become an essential tool in modern radiation metrology. Spectrometric methods provide direct access to the photon energy distribution of X-ray fields, enabling a more complete description of reference radiation qualities [5, 19].

In metrological laboratories, semiconductor detectors are commonly employed for spectrometric measurements due to their compact geometry and energy-resolving capability [11, 19]. However, the measured pulse-height spectrum is distorted by detector-specific effects such as incomplete charge collection, escape peaks, and finite energy resolution, and therefore does not directly represent the incident photon fluence spectrum [20–22]. Spectrum unfolding techniques address this limitation by combining measured spectra with detector response matrices to reconstruct the underlying photon fluence spectrum [5, 26, 27]. These response matrices are typically generated using Monte Carlo radiation transport codes and incorporate detector geometry, material composition, and non-ideal response effects [5, 22].

Within the framework of ISO 4037 reference radiation fields, unfolded spectra are used to validate beam qualities, compare radiation fields between laboratories, and support the calculation of energy-dependent conversion coefficients [5, 17, 18]. Nevertheless, achieving accurate and reproducible unfolded spectra remains challenging, particularly for high-efficiency CdTe semiconductor detectors, motivating the methodological developments presented in this thesis [5].

3.6 Identified Gaps and Motivation for This Work

Although X-ray spectrometry combined with spectrum unfolding is increasingly applied in radiation protection metrology, several relevant challenges remain unresolved in current practice [5]. Most established unfolding workflows and detector response models were originally developed for silicon-based detectors with comparatively ideal charge transport properties [11]. When transferred to high-efficiency CdTe semiconductor detectors, systematic deviations may arise due to material-specific response effects [5, 19].

CdTe detectors exhibit pronounced non-ideal characteristics, including charge trapping, incomplete charge collection, and escape peaks [20–22, 24]. While these effects are well documented, they are not consistently incorporated into detector response models used for unfolding in metrological applications. As a consequence, reconstructed photon fluence spectra may suffer from reduced accuracy and limited traceability, particularly in the low- and medium-energy range relevant to ISO 4037 reference radiation fields [5].

In addition, the quality of spectrum unfolding is influenced by the construction of the detector response matrix itself [5, 27]. In several published workflows, monoenergetic response functions are calculated using relatively coarse energy spacing, especially above approximately 30 keV. Such discretisation can degrade unfolding stability and accuracy by introducing interpolation effects in the high-energy region of the spectrum [27]. This aspect has received limited attention in CdTe-based spectrometry studies [5].

A further limitation concerns validation strategies. Many studies rely primarily on comparisons of integral beam parameters such as mean energy or half-value layer, which do not fully assess the energy-dependent accuracy of the reconstructed spectrum [2, 5, 17].

A systematic comparison between unfolded spectra, detailed detector response models, and independent Monte Carlo simulations remains insufficiently explored [5].

The present work addresses these gaps by integrating charge carrier transport (CCT) effects into CdTe detector response modelling, improving the monoenergetic energy discretisation used for response matrix generation, and applying established unfolding algorithms to experimental X-ray spectra [5, 22, 27]. Validation is performed through comparison with Monte Carlo simulations and beam quality parameters, with the aim of improving the reliability and traceability of CdTe-based X-ray spectrometry in radiation protection metrology [2, 5, 17].

3.6.1 End-point Energy Determination and Standardisation Issues

The determination of the X-ray tube end-point energy is a recognised methodological challenge in radiation protection metrology, as reflected in the ISO 16526 series, which defines several approaches for tube voltage verification [16, 31, 32]. The voltage divider method provides a direct and accurate determination of the accelerating potential, but it is invasive, costly, and often impractical in calibration laboratories, as it requires modifications to the X-ray generating system [31]. As a consequence, non-invasive alternatives are widely used in practice, including thick-filter methods and spectrometric approaches based on analysis of the high-energy tail of the X-ray spectrum [16, 32]. Spectrometric end-point determination is particularly attractive for metrology laboratories, as it can be implemented without altering the X-ray tube configuration and integrated with existing spectrometric workflows [6, 16]. However, this approach remains sensitive to detector response effects, tube current, voltage ripple, and modelling of the high-energy spectral tail [5, 6]. These limitations are not yet fully harmonised within standardised calibration frameworks and contribute to discrepancies between nominal tube voltage settings and spectrometrically derived end-point energies, motivating the development of robust and reproducible spectrometric approaches as addressed in this work [6, 16].

Relevance to the EURAMET GuideRadPROS Project: This thesis is developed within the scope and objectives of the European Association of National Metrology Institutes (EURAMET) project No. 22NRM07 (GuideRadPROS) [33], in which the LMRI participates. The project addresses the challenges introduced by the revision of ISO 4037 and the new radiation protection quantities defined in International Commission on Radiation Units and Measurements (ICRU) Report 95 by providing harmonised protocols for radiation protection measurements and calibrations. In particular, the validation of reference radiation fields and the development of spectrometric characterisation methods fall within the aims of Work Package 1 of the project [34]. The methodology and results presented in this thesis therefore constitute a direct technical contribution to the objectives of the GuideRadPROS project.

4

METHOD

This chapter describes the experimental measurements and computational workflow used to characterize ISO 4037 X-ray beams at LMRI using an XR-100T CdTe spectrometer. It covers detector calibration, spectral acquisition, and Particle and Heavy Ion Transport code System (PHITS)-based response simulations with post-processing for response matrix construction and spectrum unfolding. Unfolded photon fluence spectra obtained with MAXED and GRAVEL are compared with SpekPy reference spectra, while X-ray tube end-point energies are estimated from the measured spectra. The overall workflow is summarized in Appendix A.

4.1 Detector Calibration

All calibration measurements were performed using the XR-100T CdTe detector with fixed acquisition settings. The detector was operated at approximately 220 K and at the nominal bias voltage recommended by the manufacturer. Spectra were recorded using the Amptek Digital Pulse Processor Multi-Channel Analyzer (DppMCA) software with 4096 channels, and none of the acquisition parameters were changed during the calibration measurements. This ensured that the relationship between the incident photon spectrum and the measured detector signal remained the same for all measurements [35, 36].

4.1.1 Energy calibration and resolution

Energy calibration establishes the relationship between the Multi-Channel Analyzer (MCA) channel number and photon energy and was performed using sealed radionuclide sources ^{241}Am, ^{133}Ba, and ^{152}Eu, providing well-known photon energies spanning the range relevant to this work. Photopeak centroids were determined by Gaussian fitting applied to the high-energy side of each peak to reduce bias from low-energy tailing in CdTe detectors [21, 22]. The photopeaks used for calibration are summarized in Appendix B. A linear least-squares fit was applied, yielding

$$E\ [\text{keV}] = a\,C + b, \tag{4.1}$$

with calibration coefficients $a = (0.07461 \pm 6.07 \times 10^{-5})$ keV/channel and $b = (-0.10411 \pm 0.09644)$ keV. Higher-order correction terms were evaluated but found to be negligible

over the energy range of interest; a linear model is therefore sufficient within experimental uncertainty.

After calibration, the detector energy resolution was evaluated as a function of photon energy using the full width at half maximum (FWHM) of the photopeaks. The energy dependence of the resolution was described by an empirical model [11]:

$$\mathrm{FWHM}(E) = \alpha + \beta\sqrt{E} + \gamma E, \tag{4.2}$$

where α, β, and γ are fit parameters. For Monte Carlo post-processing, the corresponding standard deviation was obtained as

$$\sigma(E) = \frac{\mathrm{FWHM}(E)}{2\sqrt{2\ln 2}}. \tag{4.3}$$

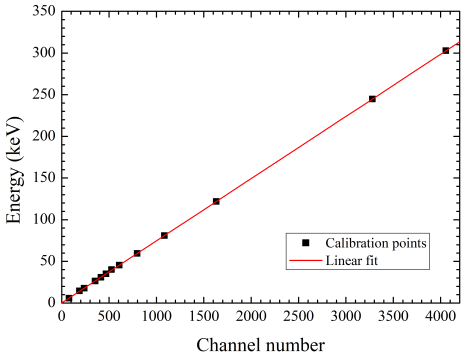

Figure 4.1: Energy calibration curve of the CdTe detector.

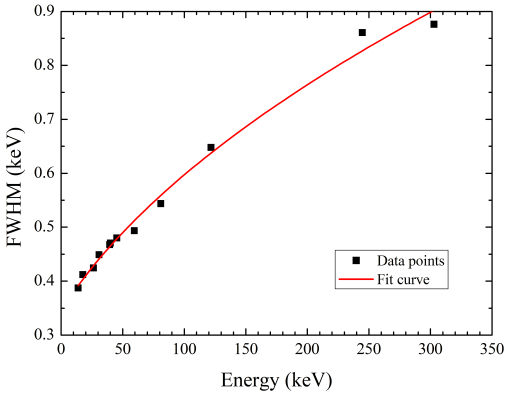

Figure 4.2: Measured energy resolution (FWHM) and fitted model, taken from [37]

The resulting calibration and resolution model define the transformation between the true photon energy spectrum and the measured detector response and are applied during Monte Carlo post-processing for response matrix construction [5].

4.2 Experimental Setup and Data Acquisition

This section describes the experimental arrangement and data acquisition procedure used to measure X-ray spectra at the LMRI. The purpose of the measurements was to obtain reproducible pulse-height spectra under controlled conditions for subsequent spectrum unfolding, end-point energy determination, and distance-dependence analysis [2, 17].

4.2.1 X-ray source and beam geometry

Measurements were performed using reference X-ray beams compliant with ISO 4037 at LMRI. For each radiation quality, the X-ray tube was operated at the nominal tube voltage and with the corresponding additional filtration defined by LMRI operating procedures. The CdTe detector was positioned on the beam axis at a defined source–detector distance

(1 m for the main dataset, and multiple distances for the N-series measurements), with collimation (lead plate with an orifice) applied to approximate narrow-beam conditions and to reduce the contribution of scattered radiation [2, 17].

4.2.2 Detector positioning and data acquisition procedure

The CdTe detector was mounted on a rigid support to maintain stable positioning throughout the measurement campaign. The source–detector distance was set using the LMRI positioning system and verified prior to acquisition. Alignment was optimized by maximizing the measured count rate while preserving a stable spectral shape. Pulse-height

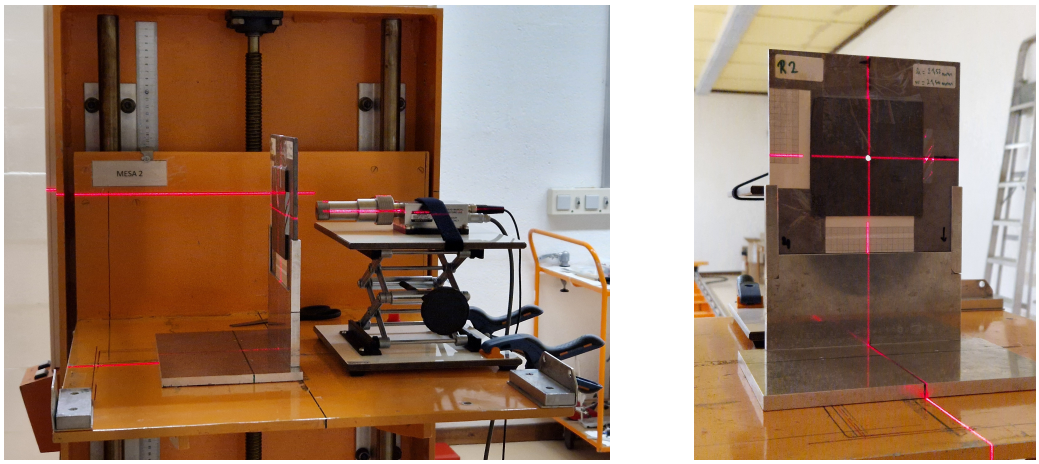

(a) Experimental setup at LMRI **(b)** CdTe detector alignment detail

Figure 4.3: Experimental setup and CdTe detector alignment used for spectral acquisition at LMRI.

spectra were acquired using the Amptek DPPMCA software with 4096 MCA channels, using the same acquisition settings established during detector calibration. For the primary dataset, a fixed acquisition time was used for all 33 spectra. For the N-series measurements, an acquisition time of 7200 s was used. Operating conditions were selected to keep dead time below 10% and to avoid pile-up distortions while maintaining identical detector and acquisition settings to those used during calibration [35, 36].

4.2.3 Data preprocessing

Recorded spectra were converted from channel space to energy space using the linear calibration relation in Section 4.1.1. Prior to subsequent analysis, invalid values were removed, spectra were sorted by energy, and the low-energy region affected by electronic noise was excluded. The resulting energy-calibrated spectra were used directly as input for the unfolding algorithms. No rebinning of the experimental spectra was done for the unfolding analysis, although rebinning is in principle possible. The matching between the experimental spectra, the response matrix, and the reference spectra is handled internally by the unfolding algorithms [5, 27].

4.2.4 Measurement campaign and dataset description

A total of 44 pulse-height spectra were acquired under different irradiation conditions. The primary dataset consists of 33 spectra measured at a fixed source–detector distance of 1 m for different ISO 4037 radiation qualities obtained by varying tube voltage and additional filtration. These spectra form the basis for detector response validation and spectrum unfolding.

An additional set of 11 N-series spectra was acquired for the ISO 4037 N80 and N100 beam qualities at source–detector distances of 1, 2, 4, and 6 m, with tube current adjusted to maintain adequate counting statistics. These measurements were used to investigate geometrical effects and detector stability and were not used for spectrum unfolding. All 44 spectra were used for end-point energy determination.

The experimental spectra extend up to approximately 305 keV, corresponding to the full MCA range of 4096 channels and the applied energy calibration (4096 channels $\times$ 0.07461 keV/channel). This upper energy limit ensures inclusion of high-energy calibration lines and is unrelated to the monoenergetic photon energies used in the Monte Carlo simulations. The response matrix is limited to incident photon energies up to 122 keV, which fully covers the ISO 4037 radiation qualities investigated.

4.3 Monte Carlo Simulation and Post-processing

Monte Carlo simulations were performed using the PHITS code to generate detector response functions for monoenergetic incident photons. The objective of the simulations was to construct a response matrix suitable for spectrum unfolding by modelling photon interactions in the detector materials. Instrumental effects related to incomplete charge collection and finite energy resolution were not simulated directly in PHITS but were introduced in a subsequent post-processing stage [5, 25].

4.3.1 PHITS detector geometry and materials

The XR-100T CdTe detector was modelled in PHITS using a geometrical representation of the detector assembly, including the CdTe sensitive volume and the main surrounding structural components. Materials such as stainless steel housing, Kovar, ceramic parts, electrodes, and the beryllium entrance window were included to account for attenuation and secondary interaction effects [19, 25].

Charge transport and electronic signal formation were not explicitly simulated in PHITS. The Monte Carlo model therefore represents an idealized detector response in terms of photon matter interactions only. A full detector assembly was modelled rather than a simplified CdTe crystal in order to account for scattering and attenuation effects in non-sensitive detector components, which significantly influence the low-energy response [19, 22]. A library of monoenergetic photon simulations was generated over the energy range relevant to the experimental measurements. Photon energies from 2 keV to 122 keV

were simulated with a step width of 0.25 keV. Energies below this range were excluded due to attenuation in the beryllium entrance window and detector dead layer.

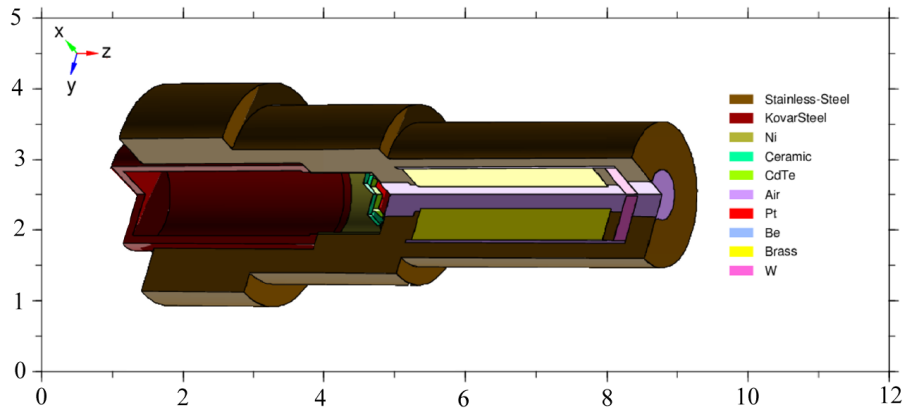

Figure 4.4: Geometrical and material model of the XR-100T CdTe detector implemented in PHITS for monoenergetic response simulations (adapted from [37]). Dimensions given in cm.

The upper limit of 122 keV was selected to fully cover the photon energy range of the investigated ISO 4037 radiation qualities, whose nominal tube voltages do not exceed 120 kVp. Extending the response matrix beyond this limit would increase matrix dimensionality and computational cost without improving unfolding performance, as photon fluence above the physical end-point is negligible. The selected energy range therefore represents a computationally efficient and physically consistent compromise compatible with the MAXED and GRAVEL implementations used (UMG 3.3) [5, 27]. For each discrete photon energy, a pencil beam directed perpendicularly onto the detector entrance face was simulated, with 10^6 primary photon histories per run to ensure stable statistics [25]. The resulting monoenergetic responses form the basis of the detector response matrix used for unfolding [5].

4.3.2 PHITS scoring and raw response spectra

Energy deposition events in the CdTe sensitive volume were scored in PHITS and exported as ASCII output files for offline processing. The scoring quantity corresponds to the total energy deposited in the active CdTe detector volume and represents the cumulative energy transferred to secondary electrons generated by photon interactions.

In PHITS terminology, photon interaction events (NCOL 13) act as triggers for energy transfer, while the deposited energy is recorded through electron energy deposition events (NCOL 14).

PHITS provides the deposited energy values in the `userdefined.dat` output without intrinsic energy binning. The discretisation of the detector response spectra was therefore introduced during post-processing. For the monoenergetic response functions used to assemble the detector response matrix, a detector-energy bin width of 0.05 keV was applied.

Because the Monte Carlo scoring records deposited energy directly in physical units, no experimental channel-to-energy calibration was required for the simulated spectra. The raw monoenergetic response spectra form the basis for subsequent post-processing and response matrix construction. This detector-energy binning should not be confused with the energy step of the monoenergetic photon simulations, which is defined independently [5, 25].

4.3.3 Post-processing: charge-collection tailing and energy resolution

The raw PHITS output represents an idealized detector response that accounts only for photon–matter interactions and does not include electronic signal formation or charge transport effects. As a result, the simulated spectra cannot be directly compared with experimentally measured pulse-height spectra [5, 22].

CdTe detectors exhibit pronounced low-energy tailing caused by incomplete charge collection, primarily due to charge trapping and carrier recombination processes. Because these effects are not modelled explicitly within PHITS, they were incorporated during post-processing using a phenomenological charge-collection tailing (CCT) model implemented in Python. The CCT model modifies the interaction energies obtained from the Monte Carlo simulations to reproduce the experimentally observed redistribution of counts toward lower energies. This approach captures the dominant macroscopic effects of incomplete charge collection without attempting a detailed microscopic simulation of charge transport [21, 23]. The numerical values of the CCT and ICC parameters applied consistently to all monoenergetic response functions are listed in Appendix C. These parameter values were taken from the manufacturer-provided CdTe detector model and applied unchanged to all monoenergetic response functions, ensuring physically consistent charge-collection behaviour across the full response matrix [23]. Following the application of charge-collection tailing, the finite detector energy resolution was modelled by Gaussian broadening of the reconstructed energies. The energy-dependent standard deviation $\sigma(E)$ was derived from the experimentally measured FWHM values obtained during detector calibration, as described in Section 4.1.1 [11].

4.3.4 Assembly of the response matrix

The detector response matrix was constructed by assembling the normalized monoenergetic response functions for all simulated photon energies. Each column of the matrix corresponds to a fixed incident photon energy E_j, while each row corresponds to a detector-energy bin E_i. For each E_j, the corresponding response function was normalized such that it represents the probability distribution of reconstructed detector energies after charge-collection tailing and energy-resolution broadening.

No additional fitting or smoothing was applied during matrix assembly; the response matrix was constructed directly from the set of processed monoenergetic response functions and formatted for use as input to the unfolding algorithms. The resulting

matrix provides the forward model linking the measured pulse-height spectrum to the unknown photon fluence spectrum, as described in Section 4.5.1 [5].

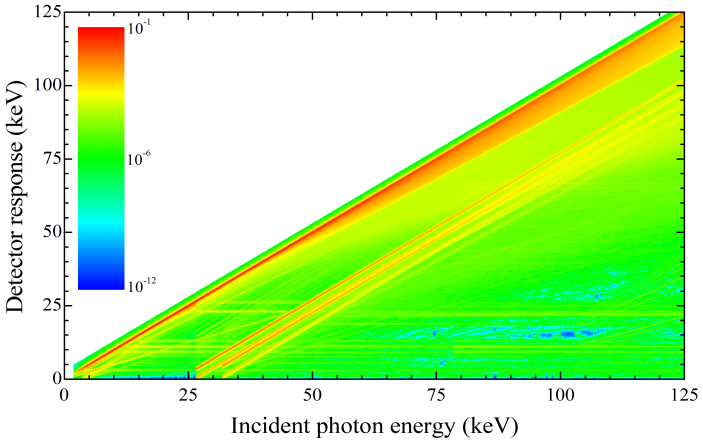

Figure 4.5: Detector response matrix $R(E_i, E_j)$ assembled from monoenergetic response functions after post-processing. The color scale indicates the average yield per incident photon.

4.4 Reference Spectrum Generation with SpekPy

Reference X-ray spectra were generated using the SpekPy software package to support the validation of the unfolding procedure and to provide physically consistent photon fluence spectra corresponding to the experimental irradiation conditions. [2, 38].

The reference spectra were not used as direct inputs for unfolding but served as independent benchmarks for comparison with unfolded spectra and for consistency checks of spectral characteristics. SpekPy provides theoretical source spectra and therefore does not account for detector-specific effects such as energy resolution or charge-collection losses [39].

4.4.1 SpekPy model and configuration

SpekPy simulations were performed exclusively using the Python interface, enabling automated spectrum generation for a large number of irradiation conditions. The X-ray tube was modelled using a tungsten anode material, consistent with the experimental setup at LMRI [38, 39].

For each simulated spectrum, the tube voltage, inherent and additional filtration, tube charge, and source-detector distance were specified to match the corresponding experimental measurement conditions. The source–detector distance parameter was used to scale the photon fluence according to inverse-square law behaviour. Material-dependent filtration parameters were defined explicitly in SpekPy to reproduce the attenuation characteristics of the experimental beam qualities [2, 38].

4.4.2 Generation of reference spectra for experimental conditions

A total of 44 reference spectra were generated, corresponding to the full experimental dataset described in Section 4.2.4. For each experimental irradiation condition, a matching SpekPy spectrum was produced using the same nominal tube voltage, filtration configuration, and measurement distance [38].

Eleven spectra correspond to a single radiation quality simulated at different source–detector distances, enabling investigation of geometrical effects on photon fluence. The remaining spectra were generated for different ISO 4037 radiation qualities at a fixed distance of 1 m, reflecting variations in tube voltage and filtration [2, 17].

4.4.3 Extraction and processing of photon fluence spectra

SpekPy outputs photon fluence spectra as a function of energy, which were extracted using custom Python scripts for further analysis. The simulated spectra were discretized on an energy grid compatible with the unfolding results to facilitate direct comparison. Photon fluence values were normalized according to tube charge and acquisition geometry to ensure direct comparability with the unfolded photon fluence spectra. No detector response effects were applied to the SpekPy spectra, as they represent ideal source spectra rather than detector-space signals [38].

4.4.4 Role of SpekPy in unfolding validation

The SpekPy-generated spectra were used as independent reference spectra to assess the physical plausibility of the unfolded photon fluence distributions obtained using the detector response matrix and unfolding algorithms [5, 39].

Comparisons focused on key spectral characteristics such as end-point energy, overall spectral shape, and relative filtration effects. Agreement between unfolded spectra and SpekPy reference spectra provides confidence in the correctness of the unfolding procedure and the response matrix construction [5].

4.5 Spectrum Unfolding Methodology

Spectrum unfolding is the process of reconstructing the true incident photon fluence spectrum from the measured detector spectrum by accounting for the detector response. In X-ray spectrometry, the measured pulse-height distribution is related to the incident photon spectrum through the detector response matrix, making the inverse problem ill-posed and sensitive to statistical fluctuations [5, 26, 27]. In this work, spectrum unfolding constitutes a central element of the methodology and was performed on 33 experimental spectra corresponding to different ISO 4037 radiation qualities measured at a fixed source–detector distance of 1 m, using two established algorithms: MAXED and GRAVEL.

4.5.1 Principles of spectrum unfolding

The measured detector spectrum $M(E_i)$ can be expressed as:

$$M(E_i) = \sum_j R(E_i, E_j)\, \Phi(E_j), \tag{4.4}$$

where $R(E_i, E_j)$ is the detector response matrix and $\Phi(E_j)$ is the unknown incident photon fluence spectrum. Unfolding aims to estimate $\Phi(E_j)$ given the measured spectrum $M(E_i)$ and the known response matrix. Due to the ill-conditioned nature of the response matrix, direct matrix inversion is not feasible, and regularized unfolding algorithms must be employed [26, 27].

4.5.2 Unfolding algorithms: MAXED and GRAVEL

Two unfolding algorithms were used in this work:

- **MAXED**, which reconstructs the photon fluence spectrum by maximizing the Shannon entropy subject to consistency constraints with the measured spectrum and its uncertainties.
- **GRAVEL**, an iterative algorithm based on successive corrections of an initial guess spectrum using a weighted least-squares approach [26, 27].

Both algorithms are widely used in radiation spectrometry and are recommended for X-ray spectrum unfolding within this framework [5].

4.5.3 Input data preparation

The unfolding inputs consist of:

- the measured detector spectra (Section 4.2),
- the detector response matrix (Section 4.3),
- statistical uncertainties of the measured pulse-height spectra (counting statistics).

The `.phs` files were generated from the experimentally measured CdTe pulse-height spectra after energy calibration and preprocessing (Section 4.2.3). Each `.phs` file contains the detector-space spectrum and its associated statistical uncertainties in the format required by UMG. The `.flu` files provide the default (prior) photon fluence spectrum and were derived from SpekPy simulations for the corresponding irradiation conditions (Section 4.4). The `.rsp` files contain the detector response matrix constructed from the PHITS-based monoenergetic simulations after post-processing (Section 4.3.4). An initial guess spectrum was required for both algorithms and was selected to ensure numerical stability without introducing bias. No manual rebinning of the experimental spectra was performed, as the bin matching between the measured spectra, the response matrix, and

the default spectra is handled internally by the MAXED and GRAVEL implementations in UMG 3.3 [5, 27].

4.5.4 UMG file-based unfolding workflow

The MAXED and GRAVEL algorithms in the UMG 3.3 package operate on three external input files: a measured spectrum (`.phs`), a default photon fluence spectrum (`.flu`), and a detector response matrix (`.rsp`). These three files together define the inverse problem that is solved by the unfolding algorithms and are identical for both MAXED and GRAVEL.

For each experimental spectrum, the corresponding `.phs`, `.flu`, and `.rsp` files were supplied to the MAXED or GRAVEL executable together with an algorithm-specific control file that defines numerical parameters such as the target χ^2, the number of iterations, and scaling options. When the unfolded spectra did not show acceptable agreement with the measured data or the SpekPy reference spectra, the target χ^2, the scaling option, and the iteration parameters in the control files were adjusted within statistically justified ranges and the unfolding was repeated. The full file-generation and execution workflow is summarized in Appendix D.

4.5.5 MAXED unfolding procedure

The MAXED algorithm reconstructs the photon fluence spectrum by maximizing the entropy function:

$$S = -\sum_j \Phi(E_j) \ln\left[\frac{\Phi(E_j)}{\Phi_0(E_j)}\right], \tag{4.5}$$

where $\Phi_0(E_j)$ is the initial guess spectrum [26].

For each unfolded spectrum, the χ^2 constraint was investigated to balance agreement with the measured detector spectrum and suppression of unphysical oscillations. The choice of the target χ^2 value followed statistical consistency criteria recommended in [27]. MAXED unfolding was applied to all 33 spectra using identical response matrices and consistent algorithm settings to allow direct comparison between different radiation qualities.

4.5.6 GRAVEL unfolding procedure

The GRAVEL algorithm reconstructs the photon fluence spectrum through an iterative update scheme starting from an initial guess spectrum. At each iteration, the spectrum is corrected based on the ratio between the measured detector spectrum and the spectrum reconstructed from the current estimate [27].

For the present work, GRAVEL was applied to the same set of 33 spectra using the same response matrix, energy grid, and initial guess spectra as in the MAXED analysis. The number of iterations was selected to achieve convergence without introducing numerical instabilities [5, 27]. The use of identical input conditions enables a direct comparison between the MAXED and GRAVEL unfolding results.

4.5.7 Normalization for spectral comparison

For comparison between unfolded spectra obtained using MAXED and GRAVEL and the reference spectra generated with SpekPy, a post-unfolding normalization was applied. Since the unfolded photon fluence spectra and the SpekPy spectra are obtained on different absolute scales, a direct comparison of absolute magnitudes is not meaningful. Therefore, each spectrum was independently normalized by its maximum fluence value within the unfolding energy range. This procedure preserves the spectral shape while removing scale differences arising from detector efficiency, acquisition conditions, and algorithm-specific scaling [5, 39].

The maximum-based normalization was applied exclusively for visualization and qualitative comparison of spectral characteristics such as end-point energy, overall spectral shape, and filtration effects. No normalization was applied to the measured pulse-height spectra prior to unfolding, and the normalization did not influence the MAXED or GRAVEL unfolding procedures.

4.5.8 Comparison strategy and quantitative shape-similarity metrics

All comparison procedures, including interpolation, normalization, and metric evaluation, were implemented using custom Python scripts.

Comparison between unfolded photon fluence spectra and theoretical reference spectra was performed using both visual inspection and quantitative metrics. Visual comparison, presented in Chapter 5, provides an intuitive assessment of end-point energy, filtration effects, and gross spectral structure, but it is inherently subjective and sensitive to plot scaling and normalization choices. To complement this qualitative evaluation, objective shape-similarity metrics were introduced to quantify spectral agreement over the full energy range.

Two complementary, scale-invariant metrics were selected: cosine similarity and the Pearson correlation coefficient. Cosine similarity measures the angular agreement between two spectral vectors and is sensitive to differences in the overall spectral shape, independently of absolute magnitude. Pearson correlation evaluates linear similarity around the mean intensity level and is particularly sensitive to correlated deviations across the spectrum. Together, these metrics provide a robust numerical assessment of global spectral agreement that complements visual inspection, especially in cases where small deviations in low-fluence regions or near the end-point are difficult to judge by eye.

For quantitative comparison, the unfolded photon fluence spectrum and the corresponding SpekPy reference spectrum were treated as discrete spectral vectors defined on a common energy grid. In the following, **a** denotes the unfolded photon fluence spectrum obtained using MAXED or GRAVEL, and **b** denotes the corresponding SpekPy reference photon fluence spectrum.

Cosine similarity is defined as [40],

$$\mathrm{CosSim}(\mathbf{a}, \mathbf{b}) = \frac{\mathbf{a} \cdot \mathbf{b}}{\|\mathbf{a}\| \, \|\mathbf{b}\|}, \tag{4.6}$$

while the Pearson correlation coefficient is given by:

$$r(\mathbf{a}, \mathbf{b}) = \frac{\sum_i (a_i - \bar{a})(b_i - \bar{b})}{\sqrt{\sum_i (a_i - \bar{a})^2} \, \sqrt{\sum_i (b_i - \bar{b})^2}}. \tag{4.7}$$

For metric evaluation, unfolded spectra were interpolated onto the SpekPy energy grid over the unfolding energy range. All spectra were normalized to unit area so that the computed metrics reflect differences in spectral shape rather than absolute fluence. The resulting cosine similarity and Pearson correlation values for the full dataset are reported in Appendix E, while their interpretation is discussed in Chapter 5.

4.6 N-series measurement protocol and yield normalization

In addition to the primary measurement dataset used for spectrum unfolding and end-point energy determination, a dedicated N-series dataset was acquired to investigate the dependence of measured spectral yield on source–detector distance and tube current. These measurements were not used for unfolding, but served as consistency checks of geometrical effects and detector linearity.

N-series spectra were recorded for the ISO 4037 N80 and N100 beam qualities at source–detector distances of 1, 2, 4, and 6 m. For a given distance, multiple tube currents were used in order to maintain adequate counting statistics and to assess the linearity of the detector response with respect to tube current.

All N-series measurements were acquired using identical detector settings and a fixed acquisition time. The measured pulse-height spectra were therefore directly comparable after normalization to tube current. Integrated spectral yield was obtained by summing the counts over the full measured energy range, and yields were expressed in units of counts per mA.

This normalization allows separation of current-dependent effects from geometrical fluence variations and enables a direct comparison of spectral shape and yield across different distances and irradiation conditions. A diagnostic summary of the N-series acquisition parameters and integrated spectral yields is provided in Appendix F.

4.7 End-Point Energy Determination

The end-point energy is the maximum photon energy present in an X-ray spectrum and is closely related to the X-ray tube accelerating potential. Although the end-point can be estimated from unfolded photon fluence spectra, an additional method was developed to obtain end-point estimates automatically and consistently for the full dataset [6, 41]. The approach used in this work has two stages. First, two analytical end-point estimators are

extracted from the high-energy tail of each spectrum. Second, a simple regression model (linear and ridge regression) is used as a calibration layer to reduce systematic bias of the analytical estimators. All steps were implemented in Python to enable automated and reproducible processing.

4.7.1 Input spectra and preprocessing

End-point estimation was performed on the full set of 44 spectra acquired during the measurement campaign. The dataset comprises 33 spectra measured at a fixed source–detector distance of 1 m (primary dataset) and 11 N-series spectra acquired for the N80 and N100 qualities at source–detector distances of 1, 2, 4, and 6 m. Each spectrum was read from CSV files containing energy in keV and the corresponding counts.

Before extracting end-point features, the spectra were preprocessed to improve numerical stability. Invalid values were removed, spectra were sorted by energy, and a light smoothing was applied using a Savitzky–Golay filter. A baseline level was estimated from the high-energy tail (median of the last 5% of points) and subtracted. After baseline subtraction, negative values were clipped to zero. This step makes the high-energy tail easier to analyze and ensures consistent behaviour across different beam qualities [41, 42].

4.7.2 Anchor energy for tail analysis

A preliminary anchor energy E_p was used to locate the end-point region. The anchor was defined by a threshold relative to the maximum spectrum intensity:

$$E_p = \max\{E_i : C(E_i) > f\, C_{\max}\}, \tag{4.8}$$

where $C_{\max}$ is the maximum count value in the spectrum and f is a fixed fraction. In this work, $f = 0.002$ was used. The anchor is not the final end-point estimate; it is only used to define consistent search windows for the analytical estimators.

4.7.3 Analytical tail estimators

Two analytical estimators were computed for each spectrum:

- **Tangent estimator ($E_{\mathbf{tan}}$):** the first derivative dC/dE was computed numerically. Within a window around the anchor energy, the point of steepest descent (most negative derivative) was identified. A straight line was then fitted locally around this point, and the end-point energy was obtained from the intersection of this line with $C = 0$ (after baseline removal).

- **Linear tail extrapolation ($E_{\mathbf{lin}}$):** a straight line was fitted to the high-energy tail below the anchor energy, using only points within a fixed fraction of the maximum intensity to avoid fitting to near-zero values. A weighted fit with weights proportional to $1/\sqrt{C}$ was used to reflect counting statistics. The end-point energy was then obtained from

the intersection of the fitted line with a background level estimate C_{bg}, computed from the upper-energy region of the spectrum.

The final analytical end-point estimate was defined as:

$$E_{max} = \max(E_{tan}, E_{lin}) , \tag{4.9}$$

which reduces the tendency of single estimators to underestimate the end-point for strongly filtered spectra.

4.7.4 Regression calibration of analytical estimates

Analytical end-point estimators extracted from spectral tails can exhibit systematic bias due to statistical noise, filtration-dependent tail curvature, and residual detector effects. To reduce this bias and improve consistency across different beam qualities, a regression calibration step was applied using the analytical estimators as input features.

For each spectrum, the feature vector was defined as

$$\mathbf{x} = [E_{tan}, E_{lin}, E_{max}] , \tag{4.10}$$

where E_{tan} and E_{lin} are the analytical tangent and linear tail extrapolation estimates, and E_{max} is their combined maximum value. The target value was the nominal tube voltage setting (kVp) associated with the irradiation condition.

Two regression models were evaluated: ordinary linear regression and ridge regression. Linear regression was used as a baseline model due to its direct interpretability and its clear physical correspondence between analytical end-point estimates and tube voltage. Ridge regression was additionally considered to mitigate potential multicollinearity between the analytical features, particularly between E_{tan}, E_{lin}, and their derived maximum E_{max}. Ridge regression stabilizes coefficient estimation by adding an ℓ_2 penalty on the regression weights, improving numerical robustness in the presence of correlated features without sacrificing model simplicity. Given the limited dataset size, both models were kept intentionally simple to avoid overfitting and to preserve physical interpretability [43, 44].

4.7.5 Training and validation strategy

Model training used an 80/20 train–test split with a fixed random seed to ensure reproducibility. In addition, 5-fold cross-validation was performed to check that model performance was not dependent on a particular data split. Model performance was evaluated using the Mean Absolute Error (MAE) and residual analysis.

The full list of spectra, the extracted features (E_{tan}, E_{lin}, E_{max}), and the assigned nominal kVp labels are provided in Appendix G. Numerical results and regression coefficients are also reported in the Appendix, while figures comparing predicted and reference values are presented in Chapter 5. The complete Python implementation of the feature extraction, regression training, and validation workflow is provided in Appendix H.

5

RESULTS AND DISCUSSION

This chapter presents the experimental and computational results obtained using the methodology described in Chapter 4. The results address detector calibration performance, validation of the CdTe detector model through Monte Carlo simulations, source–detector distance dependence for selected ISO 4037 beam qualities, end-point energy determination, and photon spectrum unfolding. All measurements were performed at the Ionizing Radiation Metrology Laboratory (LMRI), and the results are discussed with emphasis on physical interpretation, numerical limitations, and consistency with theoretical reference spectra.

5.1 Measurement and Simulation Overview

All experimental spectra were acquired with a CdTe spectrometer under controlled and reproducible conditions at LMRI. ISO 4037 beam qualities were used, with particular focus on the N80 and N100 beams for distance-dependence and end-point analyses [2]. Reference measurements with a ^{241}Am source were used to validate detector behaviour and energy-response modelling [21, 22].

Monte Carlo simulations of the detector response were carried out using PHITS. Simulated interaction energies were post-processed using the charge-collection tailing (CCT) model and the experimentally determined energy-resolution function introduced in Chapter 4 [5]. Reference spectra calculated with SpekPy were used for independent comparison and validation [39]. Together, the experimental measurements, Monte Carlo simulations, and SpekPy reference spectra provide a structured framework to separate detector-induced distortions from source-related spectral features and to assess the physical validity of the unfolding results presented in the following sections.

5.1.1 Detector Calibration Performance

The energy calibration and resolution characterization performed in Chapter 4 resulted in a stable and reproducible detector response over the full energy range relevant to this study. The linear channel-to-energy calibration showed no systematic deviations within experimental uncertainty, and the residuals remained well below the intrinsic energy

resolution of the CdTe detector [5]. These results confirm that a linear calibration model is sufficient for subsequent spectral analysis. The measured energy resolution exhibited the expected increase of the FWHM with photon energy, while the corresponding relative width decreases. At energies relevant for ISO 4037 beam qualities, the resolution was sufficient to resolve spectral features and to support reliable Monte Carlo folding and spectrum unfolding [5]. The empirical resolution model derived in Chapter 4 provided a good description of the measured data and was therefore used consistently in the post-processing of simulated spectra.

Figures 4.1 and 4.2 in Chapter 4 summarize the energy calibration curve and the measured energy resolution behaviour used throughout the analysis.

5.1.2 Simulation of Detector Effects

PHITS simulations of photoelectric interactions in the CdTe detector were post-processed using the phenomenological charge-collection tailing (CCT) model described in Chapter 4 [5]. After folding with the experimentally determined energy-dependent resolution, the simulated detector-space spectrum reproduces the measured ^{241}Am spectrum with high fidelity. Both the absolute peak position and the asymmetric peak shape, including the pronounced low-energy tail characteristic of CdTe detectors, are correctly reproduced. This agreement provides an experimental validation of the combined PHITS geometry, charge-collection tailing, and energy-resolution model used to generate the response matrix for the unfolding analysis.

Figure 5.1 compares the measured and simulated ^{241}Am spectra over the full energy range and in a detailed view of the 59.5 keV photopeak. The zoomed comparison highlights the ability of the CCT and resolution models to reproduce the asymmetric peak shape and low-energy tail observed experimentally.

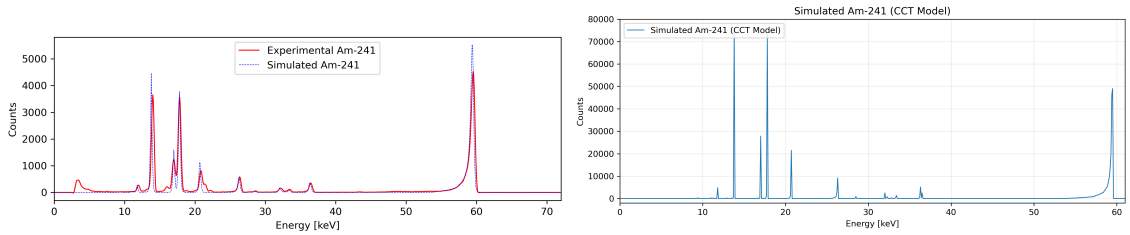

(a) Full energy-range comparison. **(b)** CCT model.

Figure 5.1: Validation of the detector response model using ^{241}Am: comparison between measured and simulated spectra after application of charge-collection tailing and energy-resolution folding.

The observed agreement confirms that the dominant detector-induced distortions—particularly charge-collection losses and resolution broadening—are quantitatively captured by the post-processing model and do not introduce significant systematic bias in the subsequent spectral unfolding.

5.2 Source–Detector Distance Dependence

Distance-dependence measurements were performed for the ISO 4037 N80 and N100 beam qualities at source–detector distances of 1, 2, 4, and 6 m. Tube current was adjusted at each distance to maintain adequate counting statistics and to avoid detector saturation. All spectra were normalized to tube current and expressed in units of counts per mA, as described in Section 4.6.

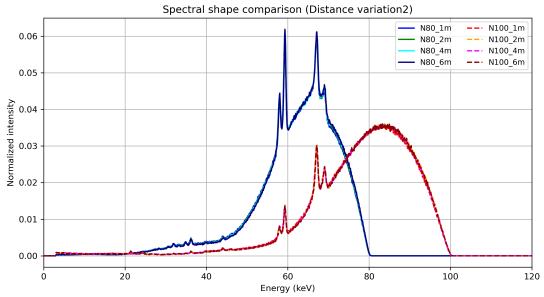

(a) Current-normalized spectra measured at different source–detector distances for the N80 and N100 beam qualities.

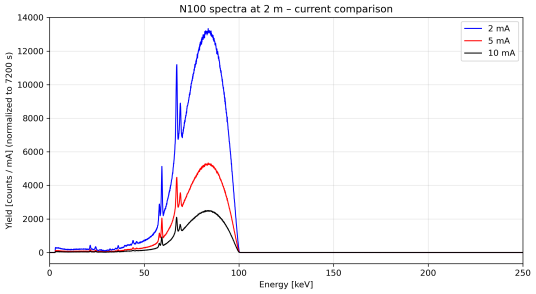

(b) N100 spectra measured at a fixed distance of 2 m for different tube currents, normalized to counts per mA.

Figure 5.2: N-series consistency checks. Left: invariance of spectral shape with source–detector distance after current normalization. Right: linear scaling of spectral yield with tube current at fixed distance, demonstrating detector linearity.

Figure 5.2 summarizes the results of the N-series measurements. For both beam qualities, the spectra recorded at different source–detector distances exhibit no statistically significant changes in spectral shape after current normalization, indicating that both the beam quality and the detector response remain invariant over the investigated geometry. The dominant effect of increasing distance is a reduction in the measured spectral yield. At a fixed distance, spectra acquired at different tube currents collapse onto a single curve after normalization to counts per mA, confirming linear detector response and negligible pile-up or saturation effects. This confirms the linearity of the detector response with tube current and validates the use of current normalization for the distance-dependence analysis. The observed decrease in intensity with distance is therefore consistent with geometrical fluence spreading. Within the statistical uncertainty of the measurements, no systematic deviation from the expected inverse-square behaviour was observed that would indicate changes in beam quality or detector response. Minor departures from ideal inverse-square scaling are attributed to air attenuation and experimental geometry. No distance-dependent shifts in energy calibration or spectral end-point were detected. Numerical values of the integrated spectral yields and current-normalized consistency checks are reported in Appendix F.

5.3 End-Point Energy Determination

Figure 5.3 summarizes the performance of the end-point energy determination for all analysed spectra. The left panel shows the predicted end-point energies as a function

of the nominal tube voltage, while the right panel presents the corresponding residuals between predicted and nominal values.

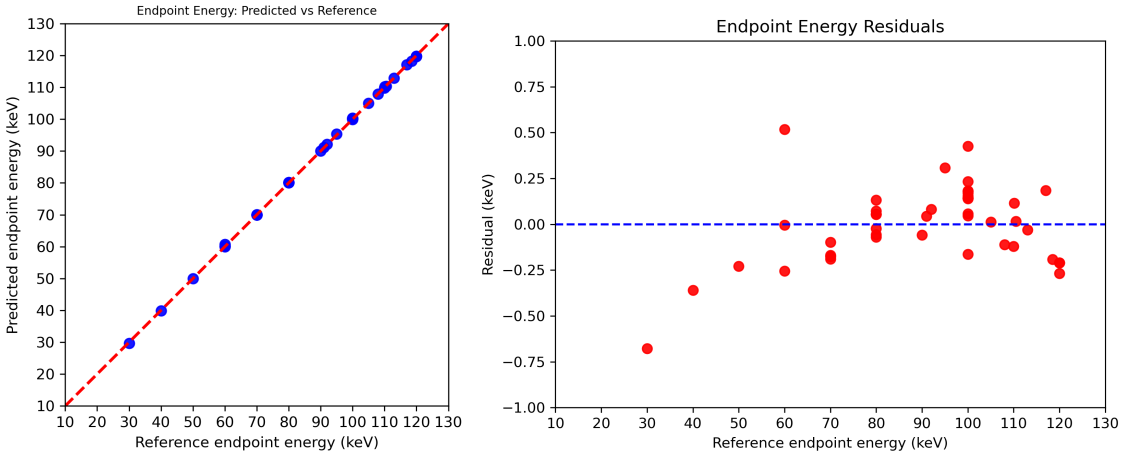

(a) Predicted end-point energy versus nominal tube voltage.

(b) Residuals between predicted and nominal end-point energies.

Figure 5.3: End-point energy determination results: comparison between predicted and nominal tube voltages (left) and corresponding residuals (right).

The predicted-versus-nominal comparison shows a close agreement with the ideal one-to-one relationship over the full investigated voltage range from 30 kV to 120 kV. No systematic deviation from linearity is observed, indicating that the end-point estimation remains accurate across different beam qualities, filtration conditions, tube currents, and source detector distances.

The residual distribution provides a quantitative measure of the prediction error relative to the nominal tube voltage settings. Residuals are symmetrically distributed around zero and exhibit no energy-dependent trend, indicating the absence of systematic bias in the end-point estimation. All deviations remain below 1 keV, with a mean absolute deviation of approximately 0.2 keV. This prediction error is small compared to the intrinsic energy resolution of the CdTe detector and well below the tolerance associated with nominal tube voltage settings, which may reach up to ±1 kV according to ISO 16526 [16].

Taken together, the two panels confirm that variations in spectral intensity and low-energy spectral shape—arising from changes in filtration, tube current, or measurement geometry—do not significantly affect the robustness of the end-point estimation. This indicates that the method is largely insensitive to detector-response distortions and beam-hardening effects, making it suitable for practical tube-voltage verification. The observed residuals are therefore dominated by statistical fluctuations and reference voltage tolerances rather than by limitations of the proposed estimation approach.

Overall, the results demonstrate that the proposed end-point energy determination achieves sub-keV accuracy under practical laboratory conditions, supporting its applicability for reliable tube voltage verification and beam quality assessment in radiation protection metrology. Complete numerical results are reported in Appendix G.

5.4 Unfolding of Photon Spectra

Photon fluence spectra were unfolded from measured CdTe pulse-height spectra using the MAXED and GRAVEL algorithms, following the methodology described in Chapter 4 [5, 27]. The same detector response matrix, energy grid, and prior information were used for both algorithms. Reference spectra generated with SpekPy were used for independent comparison. All unfolded and reference spectra shown in this section were normalized to unit maximum in order to isolate spectral shape from absolute fluence differences and to enable a meaningful comparison of spectral structure.

5.4.1 Measured spectra versus theoretical reference

Before presenting the unfolding results, Figure 5.4 compares representative measured X-ray spectra with the corresponding theoretical spectra calculated using SpekPy. These examples correspond to the same beam qualities later used to illustrate the unfolding results.

The measured spectra exhibit pronounced distortions with respect to the theoretical spectra, particularly on the low-energy side. These distortions originate primarily from detector response effects, including a continuum of escape peaks generated by incomplete charge collection. For the lower tube voltage spectrum (~50 kV), this low-energy continuum overlaps with the main part of the spectrum, producing visible bumps. At higher tube voltages (~118.5 kV), additional sharp escape peaks originating from tungsten characteristic X-rays are observed. These comparisons demonstrate the need for spectrum unfolding in order to recover the underlying photon fluence distribution.

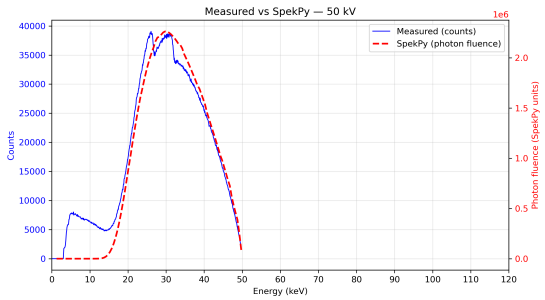

(a) Lower tube potential (~50 kV): measured spectrum vs. SpekPy.

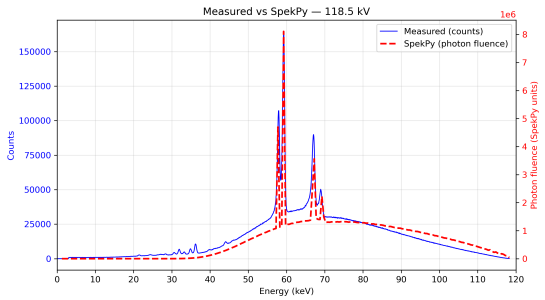

(b) Higher tube potential (~118.5 kV): measured spectrum vs. SpekPy.

Figure 5.4: Comparison between measured detector spectra and theoretical SpekPy spectra. The measured spectra show strong low-energy distortions due to detector response effects (e.g. escape-peak continuum), motivating the unfolding analysis.

5.4.2 MAXED unfolding results

Figure 5.5 presents representative photon fluence spectra unfolded using MAXED. In both cases, unfolding suppresses the low-energy contributions arising from detector response effects and reconstructs spectra that reproduce the bremsstrahlung shape and end-point energy of the SpekPy reference spectra within the resolution-limited structure

of the response matrix [26].

For the higher tube voltage case, local artefacts are visible near the major characteristic X-ray peaks as small dips around the peak regions. These features are consistent with a mismatch between the response-matrix energy mesh (0.25 keV step in the monoenergetic simulation grid) and the effective peak widths governed by the detector energy resolution (typically ~0.1 keV). Since the response matrix defines the discretization of the unfolded spectrum, the finite mesh can broaden peaks and introduce small oscillatory structures. A finer mesh (0.1–0.05 keV) would reduce these artefacts, but was not feasible within this thesis due to computational cost and matrix-size limits in the MAXED and GRAVEL implementations used [27].

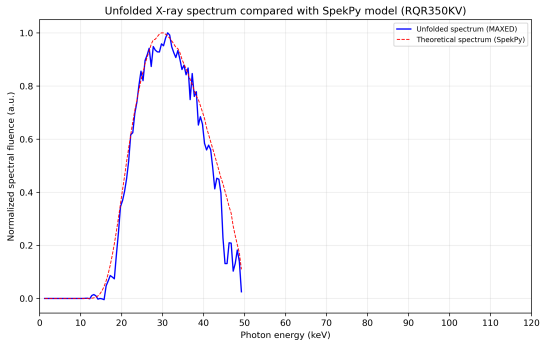

(a) Lower tube potential (~50 kV): MAXED vs. SpekPy.

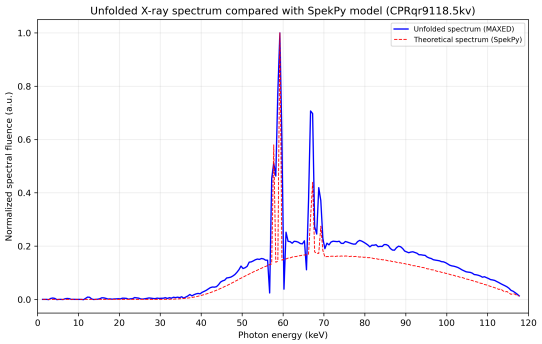

(b) Higher tube potential (~118.5 kV): MAXED vs. SpekPy.

Figure 5.5: MAXED unfolding results for representative low and high tube potentials.

5.4.3 GRAVEL unfolding results

Figure 5.6 shows the corresponding unfolding results obtained using GRAVEL. The reconstructed spectra are physically consistent and reproduce the expected bremsstrahlung distribution and end-point energy. Compared to MAXED, the GRAVEL results exhibit reduced oscillatory artefacts, particularly in the high-energy tail, which may reflect differences in the regularization behaviour of the iterative algorithm [5, 27].

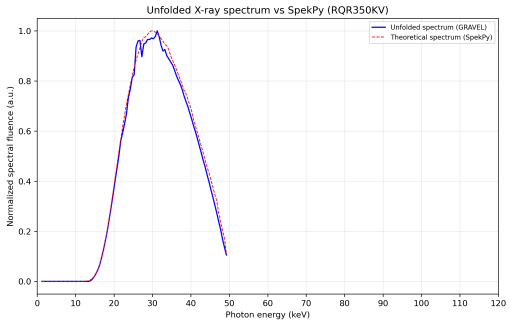

(a) Lower tube potential (~50 kV): GRAVEL vs. SpekPy.

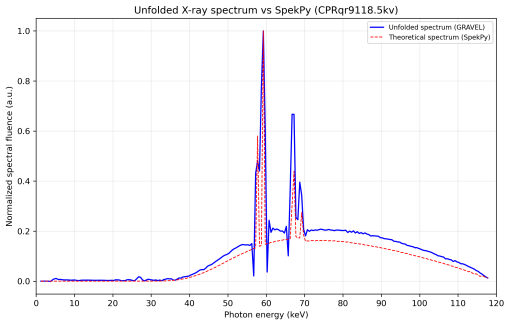

(b) Higher tube potential (~118.5 kV): GRAVEL vs. SpekPy.

Figure 5.6: GRAVEL unfolding results for representative low and high tube potentials.

5.4.4 Comparison of MAXED and GRAVEL

Figure 5.7 directly compares unfolded spectra obtained with both algorithms for identical beam qualities. In the main part of the spectrum, both methods yield similar reconstructions and follow the SpekPy reference well. Differences are mainly observed around characteristic peaks, where response-matrix discretization and the chosen normalization can influence peak heights and local structure. In practice, one must choose whether to emphasize peak-height reproduction or the overall spectral shape. In this work, emphasis is placed on correct reconstruction of the global spectral shape and the end-point energy.

This visual assessment is supported by quantitative shape-similarity metrics. For the full dataset, cosine similarity and Pearson correlation coefficients between the unfolded spectra and the corresponding SpekPy reference spectra were computed after normalization (Appendix E). For ISO RQR and RQT beam qualities, both algorithms show very high spectral agreement, whereas CPRQR beams exhibit lower similarity due to stronger low-energy detector distortions. For some CPRQR beams the unfolded spectra appear visually very close to the SpekPy reference, yet the corresponding cosine similarity and Pearson coefficients are moderate. This is caused by the fact that these metrics weight the full energy range, including the very low-fluence tails and the steep spectral cut-off near the end-point, where small relative deviations produce a large numerical penalty. In CPRQR beams the spectrum is narrow and strongly filtered, so even minor shifts of the low-energy foot or end-point position barely visible in normalized plots reduce the global vector similarity and correlation. The metrics therefore provide a more stringent, energy-wide assessment of spectral agreement than visual inspection alone. Based on its improved stability and smoother behaviour, GRAVEL was selected as the primary unfolding method for the overall dataset, with MAXED retained as an independent consistency check [5].

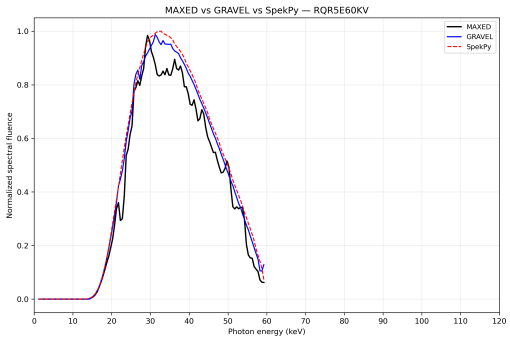

(a) Lower tube potential: MAXED vs. GRAVEL vs. SpekPy.

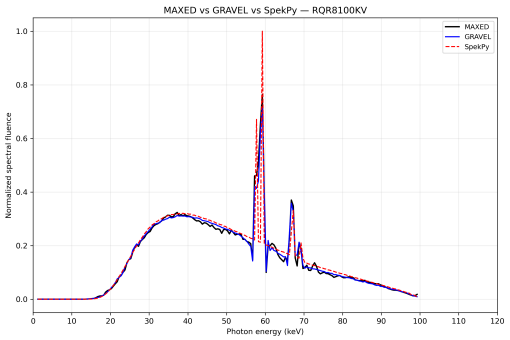

(b) Higher tube potential: MAXED vs. GRAVEL vs. SpekPy.

Figure 5.7: Direct comparison of unfolded photon fluence spectra obtained with MAXED and GRAVEL for representative beam qualities.

The complete set of unfolding comparison plots for all investigated ISO 4037 beam qualities is provided in Appendix I.

6

Conclusions

This work established and validated a complete spectrometric workflow for the characterization of X-ray beams using a CdTe detector, combining experimental calibration, Monte Carlo–based detector modelling, spectrum unfolding, and end-point energy determination. The objectives defined in Chapter 1 were fully achieved.

A full energy calibration and resolution characterization of the XR-100T CdTe detector was performed using standard radionuclide sources. The detector response was shown to be linear, stable, and well described by an empirical resolution model over the energy range relevant to ISO 4037 radiation qualities. These calibration results provided a reliable basis for all subsequent Monte Carlo post-processing and unfolding.

A physics-based detector response model was developed using PHITS and augmented with a charge-collection tailing and incomplete charge-collection model together with experimentally determined energy resolution. Validation against measured ^{241}Am spectra demonstrated that the model quantitatively reproduces the asymmetric peak shapes and low-energy tailing characteristic of CdTe detectors. This confirmed that the response matrix used for unfolding accurately represents the dominant detector effects and does not introduce significant systematic bias.

A comprehensive experimental dataset was acquired at the LMRI covering multiple ISO 4037 beam qualities, tube voltages, filtrations, and source–detector distances. Distance dependence measurements verified detector linearity and beam-quality stability, and the observed intensity variations were consistent with geometrical fluence spreading and air attenuation. This validated the experimental protocol and ensured the consistency of the spectral dataset used for unfolding and end-point analysis.

Photon fluence spectra were successfully reconstructed from measured pulse-height spectra using both MAXED and GRAVEL. Quantitative shape-similarity metrics and comparisons with SpekPy reference spectra demonstrated that both algorithms recover the bremsstrahlung distribution and end-point energy, but that GRAVEL provides systematically more stable and less oscillatory solutions. As a result, GRAVEL was identified as the preferred unfolding method for routine spectrometric analysis with CdTe

detectors under the investigated conditions.

In parallel, a physics-guided end-point energy determination method was developed that combines analytical tail-based estimators with a regression calibration layer. Using only measured spectral features, the method achieved a mean absolute error of approximately 0.2 keV relative to nominal tube voltage, well below the intrinsic detector resolution and within the tolerance of ISO 16526 voltage specifications. This demonstrates that reliable tube-voltage verification can be achieved without requiring full spectrum unfolding. In summary, this thesis provides a rigorously validated framework for X-ray beam spectrometry with CdTe detectors at the LMRI, integrating detector calibration, Monte Carlo response modelling, spectrum unfolding, and data-driven end-point estimation. The methodology directly supports the realization, verification, and monitoring of ISO 4037 radiation qualities, contributing to improved beam quality control and dosimetric accuracy.

Outlook and Future Work

The methodology established in this thesis provides several clear opportunities for future development. A finer energy grid of the detector response matrix would further improve the reconstruction of characteristic X-rays and reduce unfolding artefacts; this can be achieved by implementing a dedicated PHITS output routine and recompiling the code to reduce file size. The distance-dependence study can be extended to low-energy ISO 4037 qualities (e.g. N-20), where air attenuation is expected to introduce more pronounced spectral changes, enabling the derivation of conversion coefficients for larger distances than those currently specified. The end-point energy model would benefit from a larger training dataset, particularly at low tube voltages, and from validation with data from other laboratories to assess its robustness and generalizability. In particular, the end-point energy framework offers a clear path toward a fully automated voltage verification system: by incorporating multi-laboratory spectra and a richer set of detector- and spectrum-derived features, the induced regression model can provide robust and transferable tube-voltage prediction under varying detector conditions and filtration settings, enabling continuous, traceable monitoring without requiring full spectrum unfolding. Finally, another major future research direction is the systematic investigation of the regularization and parameter-selection strategies underlying the MAXED and GRAVEL algorithms, with the aim of extending these concepts toward a more physically informed and data-driven unfolding framework tailored to CdTe-based X-ray spectrometry. Such a framework could integrate detector-response modelling, statistical noise treatment, and spectral smoothness constraints in a unified way, providing a next-generation unfolding approach that complements the current MAXED and GRAVEL implementations. Such an approach would use the experimentally measured detector resolution, peak broadening and charge-collection tailing directly within the unfolding procedure, so that the degree of regularization adapts to the actual physical response of the CdTe detector instead of being set by fixed numerical parameters.

Bibliography

[1] João M. Lourenço. *The NOVAthesis LaTeX Template User's Manual*. NOVA University Lisbon. 2021. URL: https://github.com/joaomlourenco/novathesis/raw/main/template.pdf (cit. on p. i).

[2] International Organization for Standardization. *Radiological protection — X and gamma reference radiation for calibrating dosemeters and doserate meters and for determining their response as a function of photon energy. Part 1: Radiation characteristics and production methods*. Geneva, Switzerland, 2019 (cit. on pp. 1–3, 5–8, 12–17, 19, 20, 24, 25, 32).

[3] International Commission on Radiological Protection. *The 2007 Recommendations of the ICRP*. 2007 (cit. on pp. 1, 6, 7).

[4] International Commission on Radiation Units and Measurements. *Quantities and Units in Radiation Protection Dosimetry*. ICRU Report 51. 1993 (cit. on pp. 1, 3, 6, 7).

[5] J. Šolc et al. "Practical X-ray beam spectrometry with cadmium telluride detector. Part II: Unfolding". In: *Journal of Instrumentation* 17 (2022), P10003. DOI: 10.1088/1748-0221/17/10/P10003 (cit. on pp. 2, 7, 8, 10–13, 15–17, 19–28, 32, 33, 36–38).

[6] J. Šolc et al. "The spectrometric practical voltage: determination of X-ray tube voltage up to 300 kV". In: *Journal of Instrumentation* 20 (2025), P02013 (cit. on pp. 2, 12, 17, 29).

[7] Campus Tecnológico Nuclear (CTN). *Serviço de Proteção Radiológica*. https://www.ctn.tecnico.ulisboa.pt/sec/psr/index.html. 2024 (cit. on p. 2).

[8] Portugal. *Despacho n.º 1178/2023, de 24 de janeiro*. Diário da República. Instituto Português da Qualidade, I. P. 2023 (cit. on p. 2).

[9] Portugal. *Portaria n.º 356/2023, de 14 de novembro*. Diário da República. 2023 (cit. on p. 2).

[10] P. Andreo et al. *Fundamentals of Ionizing Radiation Dosimetry*. Wiley, 2017 (cit. on pp. 3–6).

[11] G. F. Knoll. *Radiation Detection and Measurement*. 4th ed. John Wiley & Sons, 2010 (cit. on pp. 3–6, 8, 10, 16, 19, 23).

[12] J. T. Bushberg et al. *The Essential Physics of Medical Imaging*. Lippincott Williams & Wilkins, 2011 (cit. on pp. 3–6).

[13] J. H. Hubbell and S. M. Seltzer. *Tables of X-ray Mass Attenuation Coefficients*. NIST, 1996 (cit. on pp. 3, 4).

[14] S. Miyajima. "Thin CdTe detector in diagnostic X-ray spectroscopy". In: *Medical Physics* 30 (2003), pp. 771–777 (cit. on pp. 3, 8, 10).

[15] Radiology Cafe. *Production of X-Rays*. 2024. URL: https://www.radiologycafe.com/frcr-physics-notes/x-ray-imaging/production-of-x-rays/ (cit. on pp. 4, 5).

[16] International Organization for Standardization. *Non-invasive test methods for X-ray generators. Part 3: Spectrometric method*. 2015 (cit. on pp. 6, 12, 17, 35).

[17] International Organization for Standardization. *Radiological protection — X and gamma reference radiation for calibrating dosemeters and doserate meters and for determining their response as a function of photon energy. Part 2: Dosimetry for radiation protection*. Geneva, Switzerland, 2019 (cit. on pp. 6, 7, 13–17, 19, 20, 25).

[18] International Organization for Standardization. *Radiological protection — X and gamma reference radiation for calibrating dosemeters and doserate meters. Part 3: Calibration of area and personal dosemeters*. Geneva, Switzerland, 2019 (cit. on pp. 7, 14, 16).

[19] J. Šolc et al. "Practical X-ray beam spectrometry with cadmium telluride detector. Part I: Instrumentation". In: *Journal of Instrumentation* 17 (2022), P10002. DOI: 10.1088/1748-0221/17/10/P10002 (cit. on pp. 8, 15, 16, 21).

[20] S. D. Sordo et al. "Progress in the development of CdTe and CdZnTe semiconductor radiation detectors". In: *Sensors* 9 (2009), pp. 3491–3526 (cit. on pp. 8–10, 12, 16).

[21] R. H. Redus et al. "Characterization of CdTe detectors for quantitative X-ray spectroscopy". In: *IEEE Transactions on Nuclear Science* 56 (2009), pp. 2524–2532 (cit. on pp. 8–12, 16, 18, 23, 32).

[22] A. Tomal et al. "Monte Carlo simulation of the response functions of CdTe detectors". In: *Applied Radiation and Isotopes* 100 (2015), pp. 32–37 (cit. on pp. 9–11, 13, 16–18, 21, 23, 32).

[23] Amptek Inc. *Charge Trapping in XR-100T-CdTe Cadmium Telluride Detectors: Application Note*. Amptek Inc. 2024. URL: https://www.amptek.com/internal-products/app-notes/chargetrapping-in-xr-100t-cdte-cadmium-telluride-detectors-application-note (cit. on pp. 9–11, 23).

[24] M. R. do Nascimento et al. "Intrinsic challenges in X-ray spectrometry with CdTe detectors". In: *Brazilian Journal of Radiation Sciences* 9.2C (2021), pp. 5–7 (cit. on pp. 11, 16).

[25] Tatsuhiko Sato et al. "Features of Particle and Heavy Ion Transport code System (PHITS) version 3.02". In: *Journal of Nuclear Science and Technology* 55.6 (2018), pp. 684–690. DOI: 10.1080/00223131.2017.1419890 (cit. on pp. 12, 21–23).

[26] M. Reginatto, P. Goldhagen, and S. Neumann. "Spectrum unfolding, sensitivity analysis and propagation of uncertainties with the maximum entropy deconvolution code MAXED". In: *Nuclear Instruments and Methods in Physics Research Section A* 476.1–2 (2002), pp. 242–246 (cit. on pp. 13, 16, 25–27, 37).

[27] Marcel Reginatto. *The "multi-channel" unfolding programs in the UMG package: MXD_MC33, GRV_MC33 and IQU_MC33*. Tech. rep. UMG package, version 3.3. Braunschweig, Germany: Physikalisch-Technische Bundesanstalt (PTB), 2004 (cit. on pp. 13, 16, 17, 20, 22, 25–27, 36, 37).

[28] J. T. Routti and J. V. Sandberg. "Unfolding of activation and multisphere detector data". In: *Radiation Protection Dosimetry* 10 (1985), pp. 103–105 (cit. on p. 13).

[29] International Atomic Energy Agency. *Dosimetry in Diagnostic Radiology: An International Code of Practice*. Tech. rep. 457. Vienna: IAEA, 2007 (cit. on p. 15).

[30] Australian Radiation Protection and Nuclear Safety Agency. *Quarterly Report of the Chief Executive Officer of ARPANSA*. Tech. rep. January–March 2023. Australia: ARPANSA, 2023 (cit. on p. 15).

[31] International Organization for Standardization. *Non-invasive test methods for X-ray generators. Part 1: Voltage divider method*. 2015 (cit. on p. 17).

[32] International Organization for Standardization. *Non-invasive test methods for X-ray generators. Part 2: Constancy check by thick filter method*. 2015 (cit. on p. 17).

[33] GuideRadPROS Consortium. *GuideRadPROS: Guidance for Radiation Protection Spectrometry*. EURAMET Project No. 22NRM07. Project description and work packages. 2024 (cit. on p. 17).

[34] GuideRadPROS Consortium. *Work Package 1: Validation of requirements and methods related to reference fields according to ISO 4037 and guide for spectrometry*. EURAMET Project No. 22NRM07. Project work package description. 2024 (cit. on p. 17).

[35] Amptek Inc. *XR-100CdTe User Manual*. 2019 (cit. on pp. 18, 20).

[36] Amptek Inc. *DPPMCA Display and Acquisition Software*. 2022. URL: https://www.amptek.com/software (cit. on pp. 18, 20).

[37] João Carlos Pacheco Nunes. "Espectrometria de Radiação X para Metrologia em Proteção Radiológica". MA thesis. Lisbon, Portugal: Universidade NOVA de Lisboa, 2024 (cit. on pp. 19, 22).

[38] SpekPy Developers. *SpekPy Software Toolkit*. 2022. URL: https://bitbucket.org/spekpy/spekpy_release/wiki/Home (cit. on pp. 24, 25).

[39] R. Bujila, A. Omar, and G. A. Poludniowski. "A validation of SpekPy: A software toolkit for modelling X-ray tube spectra". In: *Physica Medica* 75 (2020), pp. 44–53 (cit. on pp. 24, 25, 28, 32).

[40] Christopher D. Manning, Prabhakar Raghavan, and Hinrich Schütze. *Introduction to Information Retrieval*. See cosine similarity in the vector space model (online edition). Cambridge University Press, 2008 (cit. on p. 29).

[41] M. C. Silva et al. "Determination of the voltage applied to X-ray tubes from the bremsstrahlung spectrum". In: *Medical Physics* 27 (2000), pp. 2617–2623 (cit. on pp. 29, 30).

[42] A. Savitzky and M. J. E. Golay. "Smoothing and differentiation of data by simplified least-squares procedures". In: *Analytical Chemistry* 36 (1964), pp. 1627–1639 (cit. on p. 30).

[43] A. E. Hoerl and R. W. Kennard. "Ridge Regression: Biased Estimation for Nonorthogonal Problems". In: *Technometrics* 12.1 (1970), pp. 55–67. DOI: 10.1080/00401706.1970.10488634 (cit. on p. 31).

[44] T. Hastie, R. Tibshirani, and J. Friedman. *The Elements of Statistical Learning*. 2nd ed. Springer, 2009 (cit. on p. 31).

A

Methodological Workflow

This appendix presents the complete methodological workflow adopted in Chapter 4, summarizing the experimental measurements, Monte Carlo simulations, response matrix construction, spectrum unfolding, and validation steps.

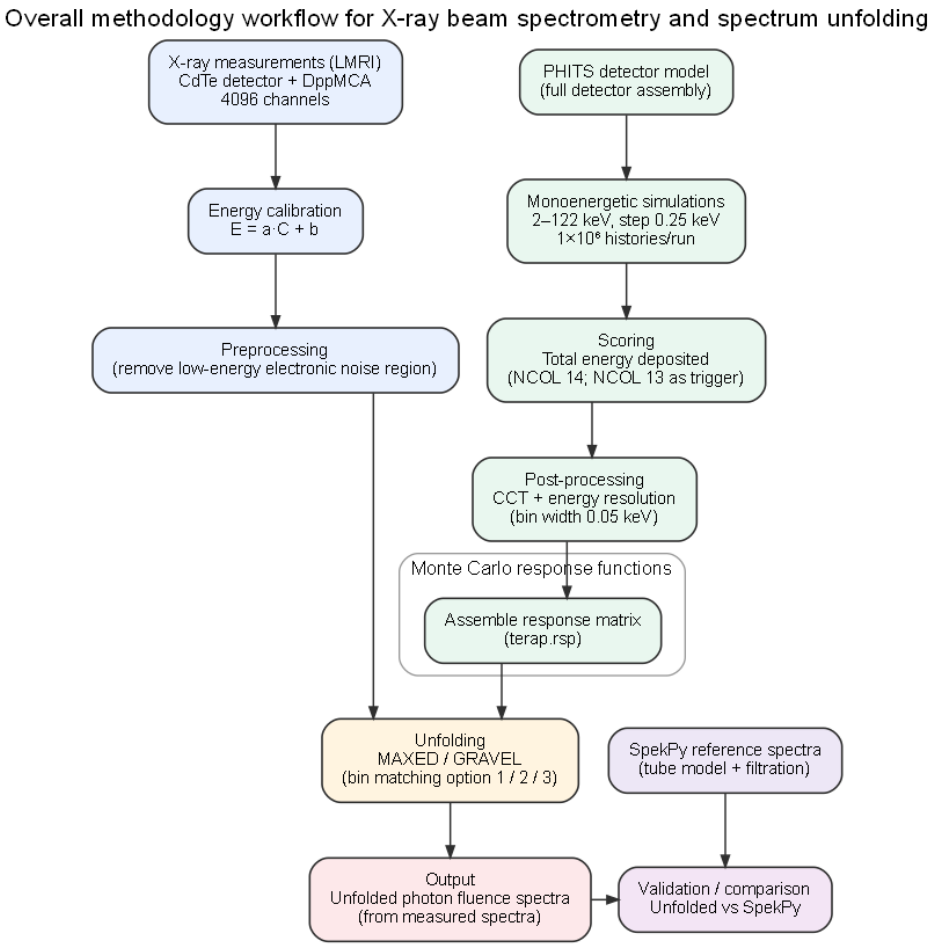

Figure A.1: Workflow of the experimental and computational methodology applied in this work, including detector calibration, spectral acquisition, PHITS-based response modelling, response matrix construction, spectrum unfolding with MAXED and GRAVEL, validation using SpekPy reference spectra, and end-point energy determination.

B

Calibration Data

Table B.1: Photopeaks used for energy calibration of the CdTe detector.

Radionuclide	Channel	Energy [keV]
^{241}Am	77.0	5.64
^{241}Am	188.0	14.44
^{241}Am	239.0	17.75
^{241}Am	353.0	26.34
^{241}Am	798.5	59.54
^{133}Ba	415.0	30.97
^{133}Ba	469.0	35.00
^{133}Ba	1084.5	81.00
^{133}Ba	4056.5	302.85
^{152}Eu	527.0	40.12
^{152}Eu	608.5	45.40
^{152}Eu	3280.0	244.70

C

Charge-Collection and Energy-Resolution Model Parameters

Table C.1: Charge-collection tailing (CCT), incomplete charge collection (ICC), and energy-resolution model parameters used for the XR-100T CdTe detector in the PHITS post-processing stage.

Parameter	Value	Description
d	0.1 cm (1 mm)	CdTe detector thickness
λ_e	11.5 cm	Electron mean free path
λ_h	0.5 cm	Hole mean free path
z_0	4.5241 cm	Reference depth parameter
R_C	0.5	Charge-loss coefficient
v_s/D	1.0×10^{-5} cm	Surface trapping parameter
a	0.05941 keV	Resolution model constant term
b	0.04555 $\text{keV}^{1/2}$	Resolution model $\sqrt{E}$ term
c	39.35 keV	Resolution model offset
N_{ch}	1200	Detector-energy channels used for response matrix
Cell ID	105	PHITS sensitive detector cell

D

UMG Spectrum Unfolding Workflow

This appendix summarizes the computational workflow used for spectrum unfolding with UMG 3.3 using the MAXED and GRAVEL algorithms. The measured detector spectrum (`.phs`), detector response matrix (`.rsp`), and default/prior spectrum (`.flu`) are provided to the unfolding executables. The two algorithms use separate control files that are identical except for Record 8, which defines the iteration parameters. The unfolded spectra are then validated against the measured data and against SpekPy reference spectra; control parameters are retuned if necessary.

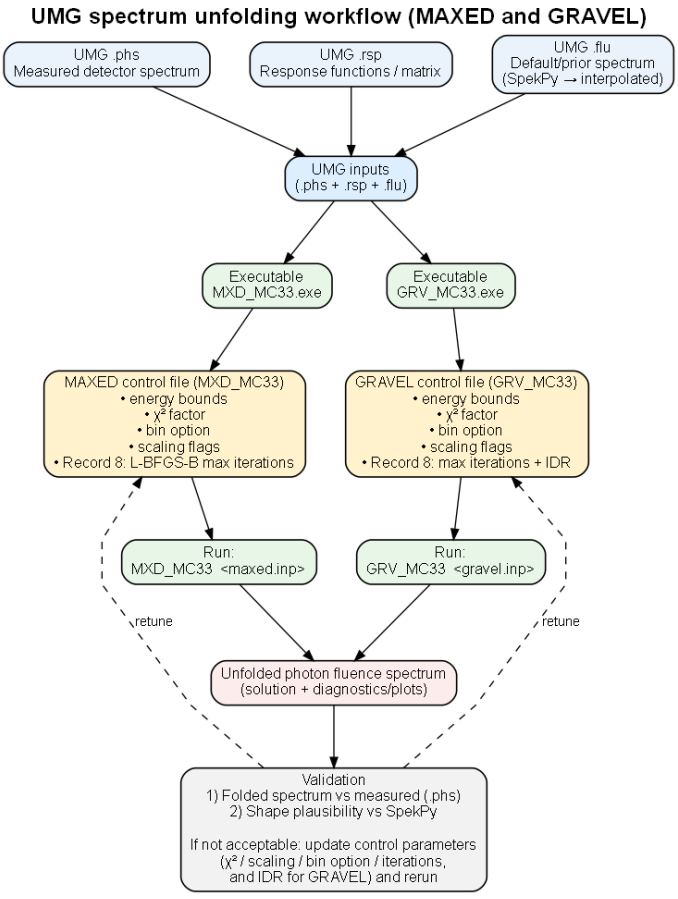

Figure D.1: UMG spectrum unfolding workflow.

E

Quantitative Shape-Similarity Metrics

Table E.1: Energy-consistent shape-similarity metrics between unfolded photon fluence spectra (GRAVEL and MAXED) and SpekPy reference spectra after interpolation onto a common energy grid and normalization to unit area.

Beam	CosSim (GRAVEL)	CosSim (MAXED)	r (GRAVEL)	r (MAXED)
CPRQR5A70KV	0.5839	0.5846	0.1866	0.1894
CPRQR5B70KV	0.4181	0.4207	-0.1587	-0.1531
CPRQR8100KV	0.5610	0.5667	0.2585	0.2649
CPRqr9105kv	0.7671	0.7692	0.6348	0.6369
CPRqr9108kv	0.7604	0.7651	0.6259	0.6313
CPRqr9113kv	0.7399	0.7454	0.5969	0.6018
CPRqr9117kv	0.7302	0.7496	0.5835	0.6045
CPRqr9118.5kv	0.7207	0.7284	0.5705	0.5796
CPRQR9120KV	0.8413	0.8412	0.7472	0.7456
RQR5A70KV	0.9991	0.9988	0.9977	0.9969
RQR5B70KV	0.9988	0.9856	0.9969	0.9654
RQR5C30KV	0.9955	0.3732	0.9925	0.0588
RQR5D40KV	0.9983	0.9828	0.9967	0.9659
RQR5E60KV	0.9989	0.9954	0.9973	0.9896
RQR5F80KV	0.9911	0.9900	0.9768	0.9741
RQR8A90KV	0.9545	0.9538	0.8912	0.8896
RQR8B91KV	0.9498	0.9545	0.8815	0.8914
RQR8C92KV	0.9464	0.9456	0.8746	0.8733
RQR8D95KV	0.9325	0.9349	0.8471	0.8508
RQR8E110KV	0.8567	0.8648	0.7272	0.7409
RQR350KV	0.9985	0.9893	0.9965	0.9789
RQR8100KV	0.9110	0.9052	0.8097	0.8009
RQR8110.1KV	0.8660	0.8685	0.7397	0.7381
RQR8110.5KV	0.7776	0.7797	0.5822	0.5819
Rqr9120kv	0.7837	0.7864	0.6655	0.6669
RQT8100KV	0.8671	0.8757	0.7571	0.7671
RQT9120KV	0.7837	0.7862	0.6655	0.6666

F

Diagnostic summary of N-series measurements

Table F.1: Summary of N80 and N100 N-series measurements, including source–detector distance, tube current, and total integrated spectral yield after time normalization.

File	Series	Distance (m)	Current (mA)	Total area
N100@1m,1mAmp.csv	N100	1.0	1.0	441 567
N100@1m,5mAmp.csv	N100	1.0	5.0	495 065
N100@2m,2mAmp.csv	N100	2.0	2.0	739 791
N100@2m,5mAmp.csv	N100	2.0	5.0	739 791
N100@2m,10mAmp.csv	N100	2.0	10.0	697 642
N100@4m,12mAmp.csv	N100	4.0	12.0	442 671
N100@6m,12mAmp.csv	N100	6.0	12.0	223 031
N80@1m,1mAmp.csv	N80	1.0	1.0	533 795
N80@2m,4mAmp.csv	N80	2.0	4.0	661 571
N80@4m,12mAmp.csv	N80	4.0	12.0	643 405
N80@6m,12mAmp.csv	N80	6.0	12.0	389 449

Acquisition parameters and integrated yield

Table F.2: Table F.1: Summary of N80 and N100 N-series measurements, including source–detector distance, tube current, and total integrated spectral yield. Acquisition time was fixed for all measurements.

Series	Distance (m)	Current (mA)	Total area (counts)	Intensity per mA (counts/mA)
N100	1.0	1.0	1.17×10^6	1.17×10^6
N100	1.0	5.0	5.83×10^6	1.17×10^6
N100	2.0	2.0	2.33×10^6	1.17×10^6
N100	2.0	5.0	5.83×10^6	1.17×10^6
N100	2.0	10.0	1.17×10^7	1.17×10^6

G

End-point energy feature table

This appendix lists the analytical end-point estimators extracted from the measured spectra and the corresponding nominal tube voltage used for regression calibration. The tangent-based estimator (E_{tan}) and the linear tail extrapolation estimator (E_{lin}) are reported for each spectrum. For spectra where the linear tail extrapolation could not be reliably computed, the corresponding entry is indicated by "–".

Table G.1: Analytical end-point estimators and corresponding nominal tube voltage for the spectra used in the regression calibration.

#	Spectrum	E_{tan} (keV)	E_{lin} (keV)	Nominal kVp
1	CPRQR5A70KV	70.05	70.10	70.0
2	CPRQR5B70KV	70.09	70.07	70.0
3	CPRQR8100KV	99.09	99.44	100.0
4	CPRQR9120KV	118.59	118.97	120.0
5	CPRqr9105kv	103.84	104.41	105.0
6	CPRqr9108kv	106.98	107.34	108.0
7	CPRqr9113kv	111.73	112.25	113.0
8	CPRqr9117kv	115.12	116.14	117.0
9	CPRqr9118.5kv	117.23	117.59	118.5
10	N100@1m,1mAmp	99.83	99.89	100.0
11	N100@1m,5mAmp	99.85	99.80	100.0
12	N100@2m,10mAmp	99.83	99.83	100.0
13	N100@2m,2mAmp	99.91	99.92	100.0
14	N100@2m,5mAmp	99.91	99.92	100.0
15	N100@4m,12mAmp	99.86	99.91	100.0
16	N100@6m,12mAmp	99.85	99.91	100.0
17	N80@1m,1mAmp	80.03	80.02	80.0
18	N80@2m,4mAmp	80.10	80.10	80.0
19	N80@4m,12mAmp	80.08	80.04	80.0
20	N80@6m,12mAmp	80.13	80.07	80.0

#	Spectrum	$E_{\tan}$ (keV)	E_{lin} (keV)	Nominal kVp
21	RQR350KV	50.33	50.39	50.0
22	RQR5A70KV	70.09	70.07	70.0
23	RQR5B70KV	70.11	70.17	70.0
24	RQR5C30KV	30.32	–	30.0
25	RQR5D40KV	40.29	40.40	40.0
26	RQR5E60KV	60.14	60.19	60.0
27	RQR5F80KV	79.75	79.96	80.0
28	RQR8100KV	98.78	99.47	100.0
29	RQR8110.1KV	108.02	109.20	110.1
30	RQR8110.5KV	109.71	109.55	110.5
31	RQR8A90KV	89.27	89.68	90.0
32	RQR8B91KV	89.96	90.63	91.0
33	RQR8C92KV	90.79	91.58	92.0
34	RQR8D95KV	93.68	94.66	95.0
35	RQR8E110KV	109.15	109.01	110.0
36	RQT8100KV	98.20	99.35	100.0
37	RQT9120KV	117.65	118.69	120.0
38	Rqr9120kv	117.65	118.69	120.0
39	oldexp100	99.99	99.91	100.0
40	oldexp60	60.27	60.74	60.0
41	oldexp80	80.13	80.17	80.0
42	smooth100	99.95	99.99	100.0
43	smooth60	60.27	60.19	60.0
44	smooth80	80.15	80.14	80.0

H

Python Implementation of End-Point Energy Estimation and Regression

```python
#=========================================================================
# This script implements:
#   (i) loading measured spectra from CSV files,
#   (ii) preprocessing (sorting, optional smoothing, baseline removal),
#   (iii) anchor definition using a fixed threshold fraction (f = 0.002),
#   (iv) analytical end-point estimators (Etan and Elin),
#   (v) regression calibration using Linear Regression and RidgeCV,
#   (vi) honest evaluation on a held-out test set,
#   (vii) 5-fold out-of-fold residual validation,
#   (viii) prediction for one selected spectrum.
# ========================================================================


# ========================================================================
# STEP 1 - Import required libraries
# ========================================================================

import numpy as np                      # numerical arrays and mathematical operations are provided
import pandas as pd                     # tables and CSV I/O are provided
import os                               # folder/path utilities are provided
import glob                             # wildcard file search is provided
from pathlib import Path                # safe extraction of file stem names is provided
import matplotlib.pyplot as plt          # plots are produced

from scipy.signal import savgol_filter  # Savitzky-Golay smoothing is provided

from sklearn.model_selection import train_test_split  # train/test split is provided
from sklearn.model_selection import KFold             # k-fold cross-validation splits are provided
from sklearn.linear_model import LinearRegression     # baseline linear regression is provided
from sklearn.linear_model import RidgeCV              # Ridge regression with CV alpha selection is
↪  provided
from sklearn.metrics import r2_score                  # R² metric is provided
from sklearn.metrics import mean_absolute_error       # MAE metric is provided


# ========================================================================
# STEP 2 - Define user settings (paths and constants)
# ========================================================================

```

```
DATA_FOLDER = r"E:\xray10102025\DATAFILECSV"   # folder containing spectrum CSV files is specified
ANCHOR_FRACTION = 0.002                       # anchor fraction f for Ep definition is fixed (recommended value)
USE_SMOOTHING = True                          # smoothing is enabled/disabled for numerical stability checks
SG_WINDOW = 31                                # smoothing window length is specified (odd length is required)
SG_POLYORDER = 3                              # smoothing polynomial order is specified
TAIL_FRAC = 0.05                              # last 5% of points are used for baseline estimation
TEST_SIZE = 0.20                              # 80/20 split is defined
RANDOM_STATE = 42                             # random seed is fixed for reproducibility
RIDGE_ALPHAS = [0.01, 0.1, 1.0, 10.0, 100.0]  # ridge regularization strengths are enumerated
N_FOLDS = 5                                   # number of folds for cross-validation is fixed
UNSEEN_NAME = "CPRQR8100KV"                   # one spectrum is selected for single-sample prediction demo


# ============================================================================
# STEP 3 - Define nominal kVp labels (filename → kVp mapping)
# ============================================================================
# The mapping below must be replaced by the complete thesis mapping already used.
# Keys must match: filename stem converted to lowercase and stripped.

kvp_map = {
    # ---------------------------
    # PASTE THE FULL REAL MAP HERE
    # ---------------------------
    # "rqr5c30kv": 30.0,
    # "rqr5d40kv": 40.0,
    # "rqr350kv": 50.0,
    # "rqr5e60kv": 60.0,
    # "rqr5a70kv": 70.0,
    # "rqr5f80kv": 80.0,
    # "cprqr8100kv": 100.0,
    # "rqt9120kv": 120.0,
}

if len(kvp_map) == 0:                                    # missing label map is detected
    raise ValueError("kvp_map is empty. Paste the full mapping.") # execution is stopped until labels are provided


# ============================================================================
# STEP 4 - Load all spectra from CSV files
# ============================================================================

csv_files = glob.glob(os.path.join(DATA_FOLDER, "*.csv"))        # all CSV files in the folder are collected

if len(csv_files) == 0:                                  # absence of data is checked
    raise FileNotFoundError(f"No CSV files found in {DATA_FOLDER}") # execution is stopped if none exist

spectra = []                                             # list is created to store (name, E, C)

for f in csv_files:                                      # each file is processed
```

```
    name = Path(f).stem                                    # filename stem is taken as spectrum identifier
    df = pd.read_csv(f, sep=None, engine="python")         # CSV is read using automatic delimiter detection
    df.columns = ["Energy_keV", "Counts"]                  # two-column format is enforced
    E = df["Energy_keV"].to_numpy(float)                   # energy axis is converted to float array
    C = df["Counts"].to_numpy(float)                       # counts are converted to float array
    spectra.append((name, E, C))                           # loaded spectrum is stored

print(f"Loaded {len(spectra)} spectra")                    # number of loaded spectra is printed


# ============================================================================
# STEP 5 - Define preprocessing (sorting, smoothing, baseline subtraction)
# ============================================================================

def preprocess_spectrum(E, C):
    E = np.asarray(E, float)                               # energy array is enforced
    C = np.asarray(C, float)                               # count array is enforced

    mask = np.isfinite(E) & np.isfinite(C) & (C >= 0)      # invalid and negative values are rejected
    E = E[mask]                                            # energy is filtered
    C = C[mask]                                            # counts are filtered

    idx = np.argsort(E)                                    # sorting indices are computed
    E = E[idx]                                             # energy is sorted
    C = C[idx]                                             # counts are sorted accordingly

    if USE_SMOOTHING and len(C) >= 7:                      # smoothing is applied only if enough points exist
        win = SG_WINDOW | 1                                # odd window length is enforced
        if win >= len(C):                                  # window is reduced if spectrum is shorter
            win = max(5, (len(C) // 3) | 1)                # a valid smaller odd window is chosen
        poly = min(SG_POLYORDER, win - 2)                  # polyorder is constrained to remain valid
        C = savgol_filter(C, window_length=win, polyorder=poly)  # Savitzky-Golay smoothing is applied

    k = max(3, int(TAIL_FRAC * len(C)))                    # number of tail points is computed
    baseline = float(np.median(C[-k:]))                    # baseline is estimated from the tail median
    C = C - baseline                                       # baseline is subtracted
    C[C < 0] = 0.0                                         # negative values are clipped to zero

    return E, C                                            # preprocessed spectrum is returned


# ============================================================================
# STEP 6 - Define anchor energy Ep using threshold fraction f
# ============================================================================

```

```python
def anchor_energy(E, C, frac=ANCHOR_FRACTION):
    if len(C) == 0:                                          # empty spectrum is checked
        return np.nan
    Cmax = float(np.max(C))                                  # maximum count is computed
    if Cmax <= 0:                                            # degenerate spectrum is checked
        return np.nan
    thr = frac * Cmax                                        # absolute threshold is computed
    idx = np.where(C > thr)[0]                               # indices above threshold are
    ↪ identified
    if len(idx) == 0:                                        # missing threshold crossing is
    ↪ checked
        return np.nan
    return float(E[idx[-1]])                                 # Ep is taken as last energy above
    ↪ threshold


# ============================================================================
# STEP 7 - Define analytical estimators (Etan and Elin)
# ============================================================================

def tangent_method(E, C, Ep):
    if not np.isfinite(Ep):                                  # invalid anchor is rejected
        return np.nan

    dC = np.gradient(C, E)                                   # derivative dC/dE is computed
    i = int(np.argmin(dC))                                   # steepest descent index is selected

    a = max(0, i - 12)                                       # left fit boundary is defined
    b = min(len(E), i + 12)                                  # right fit boundary is defined
    if (b - a) < 3:                                          # minimum points for linear fit are
    ↪ enforced
        return np.nan

    m, q = np.polyfit(E[a:b], C[a:b], 1)                     # local line fit C = mE + q is
    ↪ computed
    if not np.isfinite(m) or m >= 0:                         # non-physical slope is rejected
        return np.nan

    return float(-q / m)                                     # end-point is extrapolated at C=0


def linear_method(E, C, Ep):
    if not np.isfinite(Ep):                                  # invalid anchor is rejected
        return np.nan

    mask = (E >= (Ep - 10.0)) & (E <= (Ep - 2.0))            # tail window below Ep is selected
    if np.sum(mask) < 3:                                     # minimum points for fitting are
    ↪ enforced
        return np.nan

    m, q = np.polyfit(E[mask], C[mask], 1)                   # tail line fit C = mE + q is
    ↪ computed
    if not np.isfinite(m) or m >= 0:                         # non-physical slope is rejected
        return np.nan

    return float(-q / m)                                     # end-point is extrapolated at C=0


```

```python
# ============================================================================
# STEP 8 - Extract features (Etan, Elin) and assign nominal kVp labels
# ============================================================================

rows = []                                                    # list for feature rows is created

for name, E0, C0 in spectra:                                 # all spectra are processed
    E, C = preprocess_spectrum(E0, C0)                       # preprocessing is applied
    Ep = anchor_energy(E, C)                                 # anchor energy Ep is computed
    Etan = tangent_method(E, C, Ep)                          # tangent estimator Etan is computed
    Elin = linear_method(E, C, Ep)                           # linear estimator Elin is computed

    if not np.isfinite(Etan) and np.isfinite(Elin):          # fallback is applied if Etan failed
        Etan = Elin
    if not np.isfinite(Elin) and np.isfinite(Etan):          # fallback is applied if Elin failed
        Elin = Etan

    file_key = str(name).strip().lower()                     # filename key is standardized
    label = kvp_map.get(file_key, np.nan)                    # nominal kVp label is retrieved

    rows.append([name, Ep, Etan, Elin, label])               # the feature row is stored

feat_df = pd.DataFrame(rows, columns=["File", "Ep_keV", "Etan_keV", "Elin_keV", "kVp_nominal"])  # table is built
feat_df = feat_df.dropna(subset=["Etan_keV", "Elin_keV", "kVp_nominal"]).reset_index(drop=True)  # invalid rows removed

print(f"Usable labeled spectra: {len(feat_df)}")             # usable dataset size is printed
display(feat_df.head(10))                                    # first rows are displayed


# ============================================================================
# STEP 9 - Build regression dataset (X, y) and split into train/test
# ============================================================================

X = feat_df[["Etan_keV", "Elin_keV"]].to_numpy(float)        # independent features (Etan, Elin) are defined
y = feat_df["kVp_nominal"].to_numpy(float)                   # target variable (nominal kVp) is defined

X_train, X_test, y_train, y_test = train_test_split(         # train/test split is performed
    X, y, test_size=TEST_SIZE, shuffle=True, random_state=RANDOM_STATE
)


# ============================================================================
# STEP 10 - Train regression models (Linear Regression and RidgeCV)
# ============================================================================

lr_model = LinearRegression()                                # linear regression model is initialized
lr_model.fit(X_train, y_train)                               # model is fitted on training data

ridge_model = RidgeCV(alphas=RIDGE_ALPHAS, cv=5)             # ridge model with alpha selection is initialized
ridge_model.fit(X_train, y_train)                            # ridge model is fitted on training data

```

```
235
236 # ============================================================================
237 # STEP 11 - Honest evaluation on the test set (NO data leakage)
238 # ============================================================================
239
240 y_pred_lr = lr_model.predict(X_test)                                # linear regression predictions on
    ↪ test set are computed
241 y_pred_rg = ridge_model.predict(X_test)                             # ridge predictions on test set are
    ↪ computed
242
243 print("\nLinear Regression (TEST SET)")                             # header is printed
244 print(f"R²  = {r2_score(y_test, y_pred_lr):.6f}")                   # R² is printed
245 print(f"MAE = {mean_absolute_error(y_test, y_pred_lr):.6f} kV")     # MAE is printed
246
247 print("\nRidgeCV (TEST SET)")                                       # header is printed
248 print(f"alpha = {ridge_model.alpha_}")                             # selected alpha is printed
249 print(f"R²  = {r2_score(y_test, y_pred_rg):.6f}")                   # R² is printed
250 print(f"MAE = {mean_absolute_error(y_test, y_pred_rg):.6f} kV")     # MAE is printed
251
252
253 # ============================================================================
254 # STEP 12 - Plot predicted vs nominal kVp (test set only)
255 # ============================================================================
256
257 xmin = 10 * np.floor(min(y_test.min(), y_pred_rg.min()) / 10)       # axis minimum is set on a 10 kV
    ↪ grid
258 xmax = 10 * np.ceil (max(y_test.max(), y_pred_rg.max()) / 10)       # axis maximum is set on a 10 kV
    ↪ grid
259 ticks = np.arange(xmin, xmax + 10, 10)                             # tick marks are defined
260
261 plt.figure(figsize=(5.8, 5.8))                                     # square figure is created
262 plt.scatter(y_test, y_pred_rg, s=55, alpha=0.85)                   # test points are plotted
263 plt.plot([xmin, xmax], [xmin, xmax], linestyle="--", linewidth=1.5)  # ideal line y=x is plotted
264 plt.gca().set_aspect("equal", adjustable="box")                    # equal scaling is enforced
265 plt.xlim(xmin, xmax); plt.ylim(xmin, xmax)                         # axis limits are applied
266 plt.xticks(ticks); plt.yticks(ticks)                               # ticks are applied
267 plt.xlabel("Nominal kVp (test)")                                   # x label is added
268 plt.ylabel("Predicted kVp (test)")                                 # y label is added
269 plt.title("RidgeCV: Predicted vs Nominal kVp (Test Set)")          # title is added
270 plt.grid(False)                                                    # grid is disabled
271 plt.tight_layout()                                                 # layout is adjusted
272 plt.show()                                                         # plot is shown
273
274
275 # ============================================================================
276 # STEP 13 - Plot residuals (test set only)
277 # ============================================================================
278
279 res_test = y_pred_rg - y_test                                      # residuals are computed
280
281 plt.figure(figsize=(6.8, 3.6))                                     # wide figure is created
282 plt.scatter(y_test, res_test, s=55, alpha=0.85)                    # residuals are plotted
283 plt.axhline(0, linestyle="--", linewidth=1.2)                      # zero line is plotted
284 plt.xlim(xmin, xmax)                                               # x limits are applied
285 plt.xticks(ticks)                                                  # ticks are applied
286 plt.xlabel("Nominal kVp (test)")                                   # x label is added
287 plt.ylabel("Residual (kV)")                                        # y label is added
288 plt.title("RidgeCV: Residuals (Test Set)")                         # title is added
```

```
plt.grid(False)                                                    # grid is disabled
plt.tight_layout()                                                 # layout is adjusted
plt.show()                                                         # plot is shown


# ============================================================================
# STEP 14 - 5-fold out-of-fold (OOF) validation using RidgeCV
# ============================================================================

kf = KFold(n_splits=N_FOLDS, shuffle=True, random_state=RANDOM_STATE)  # CV splits are defined
y_oof = np.full_like(y, np.nan, dtype=float)                       # OOF prediction array is
↪  initialized

for tr_idx, te_idx in kf.split(X):                                 # folds are iterated
    m = RidgeCV(alphas=RIDGE_ALPHAS, cv=5)                          # ridge model is created for this
    ↪  fold
    m.fit(X[tr_idx], y[tr_idx])                                    # fold model is trained
    y_oof[te_idx] = m.predict(X[te_idx])                            # fold predictions are stored

r2_oof = r2_score(y, y_oof)                                        # OOF R² is computed
mae_oof = mean_absolute_error(y, y_oof)                             # OOF MAE is computed

print("\nRidgeCV (5-fold OOF)")                                    # header is printed
print(f"R²  = {r2_oof:.6f}")                                        # OOF R² is printed
print(f"MAE = {mae_oof:.6f} kV")                                    # OOF MAE is printed

plt.figure(figsize=(6.8, 3.6))                                     # figure is created
plt.scatter(y, y_oof - y, s=55, alpha=0.85)                         # OOF residuals are plotted
plt.axhline(0, linestyle="--", linewidth=1.2)                       # zero line is plotted
plt.xlabel("Nominal kVp")                                          # x label is added
plt.ylabel("Residual (kV)")                                        # y label is added
plt.title("RidgeCV: Residuals (5-fold Out-of-Fold)")               # title is added
plt.grid(False)                                                    # grid is disabled
plt.tight_layout()                                                 # layout is adjusted
plt.show()                                                         # plot is shown


# ============================================================================
# STEP 15 - Example prediction for one spectrum already loaded
# ============================================================================

if UNSEEN_NAME in feat_df["File"].values:                          # presence of spectrum is checked
    r = feat_df.loc[feat_df["File"] == UNSEEN_NAME].iloc[0]        # matching row is extracted
    x0 = np.array([[r["Etan_keV"], r["Elin_keV"]]], dtype=float)    # feature vector is built
    pred = float(ridge_model.predict(x0)[0])                       # predicted kVp is computed
    print(f"\nPrediction for {UNSEEN_NAME}")                        # header is printed
    print(f"Predicted kVp = {pred:.2f} kV")                        # predicted value is printed
else:
    print(f"\nPrediction skipped: {UNSEEN_NAME} not found.")       # message is printed if missing
```

I

Complete Unfolding Comparison Plots

This appendix presents the complete set of photon fluence spectrum comparisons obtained using the MAXED and GRAVEL unfolding algorithms together with the corresponding SpekPy reference spectra.

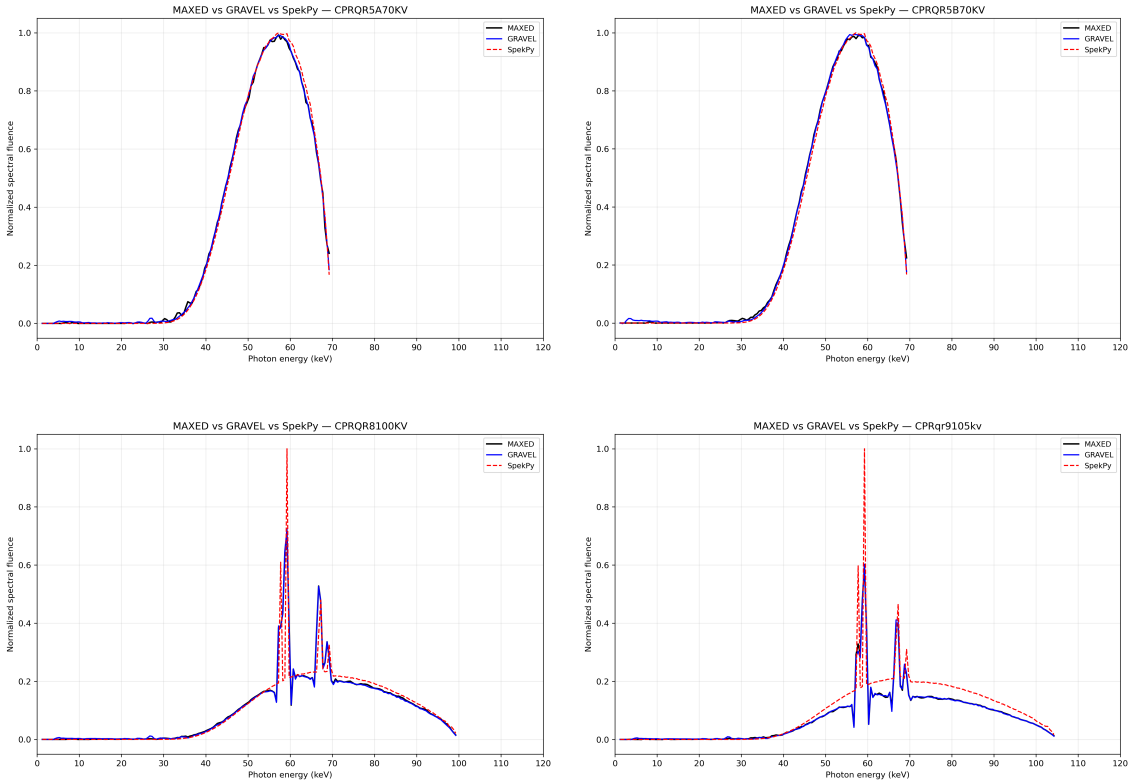

Figure I.1: Comparison of unfolded spectra obtained with MAXED and GRAVEL against SpekPy reference spectra.

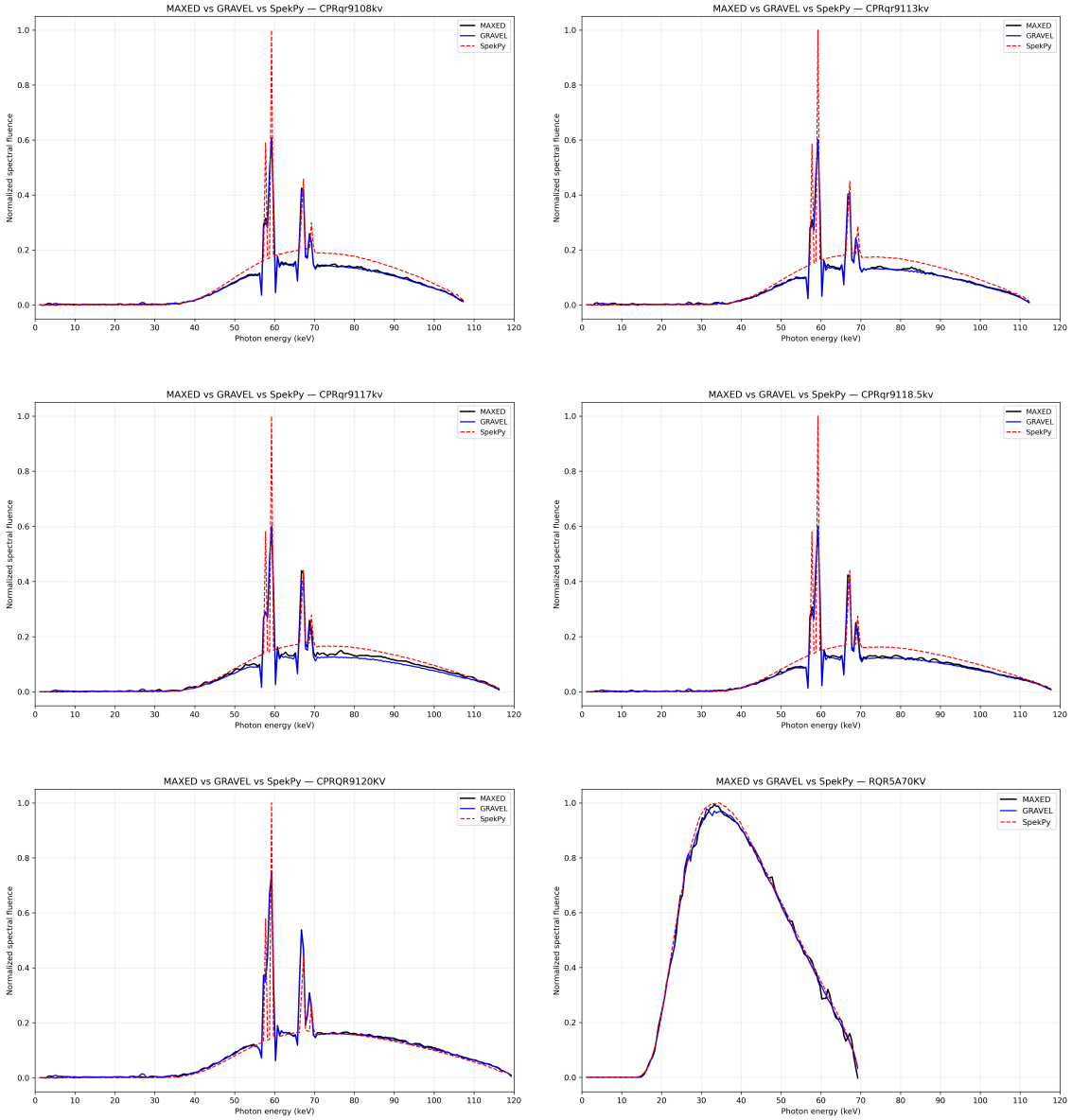

Figure I.2: Comparison of unfolded spectra obtained with MAXED and GRAVEL against SpekPy reference spectra.

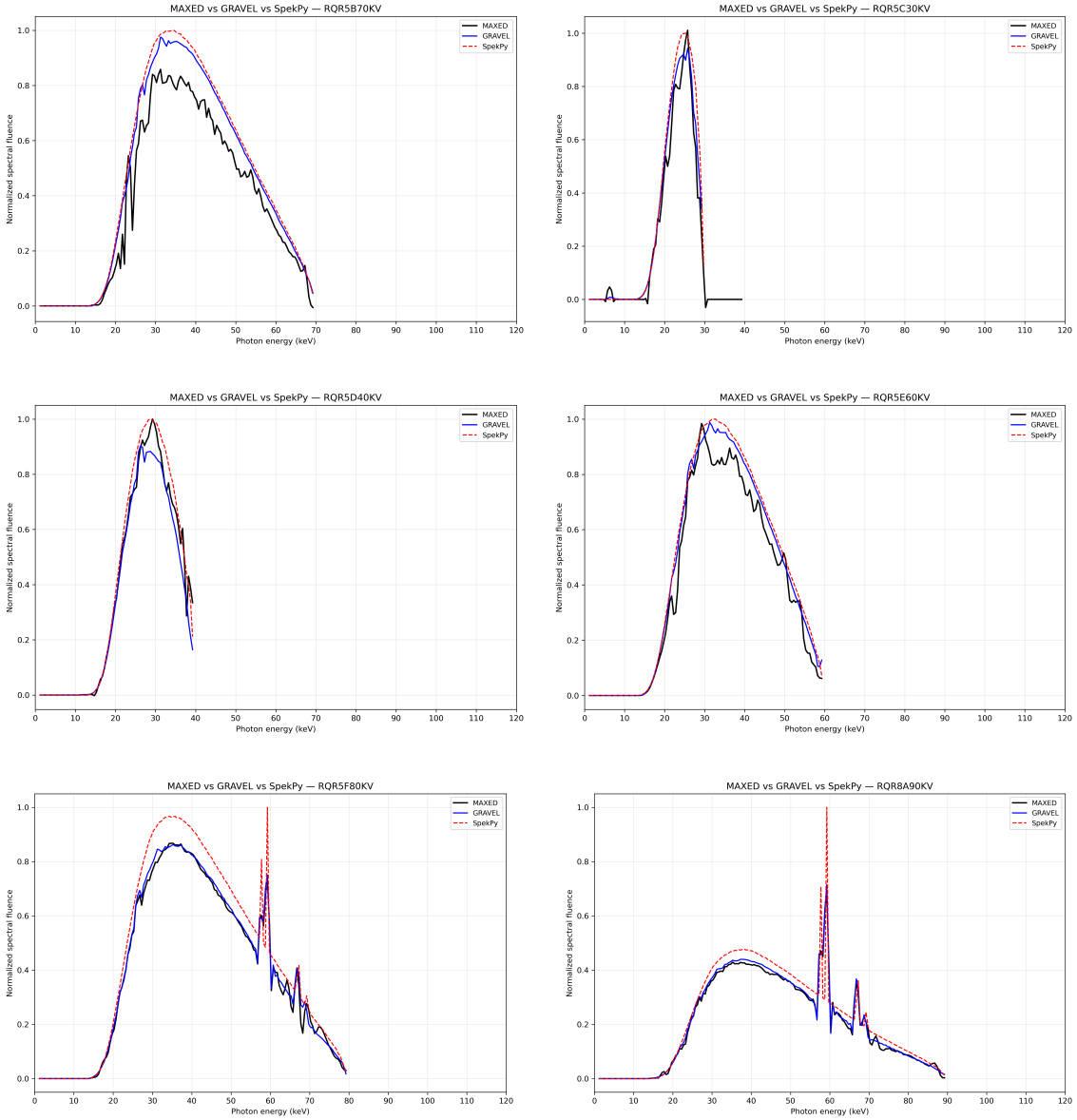

Figure I.3: Comparison of unfolded spectra obtained with MAXED and GRAVEL against SpekPy reference spectra.

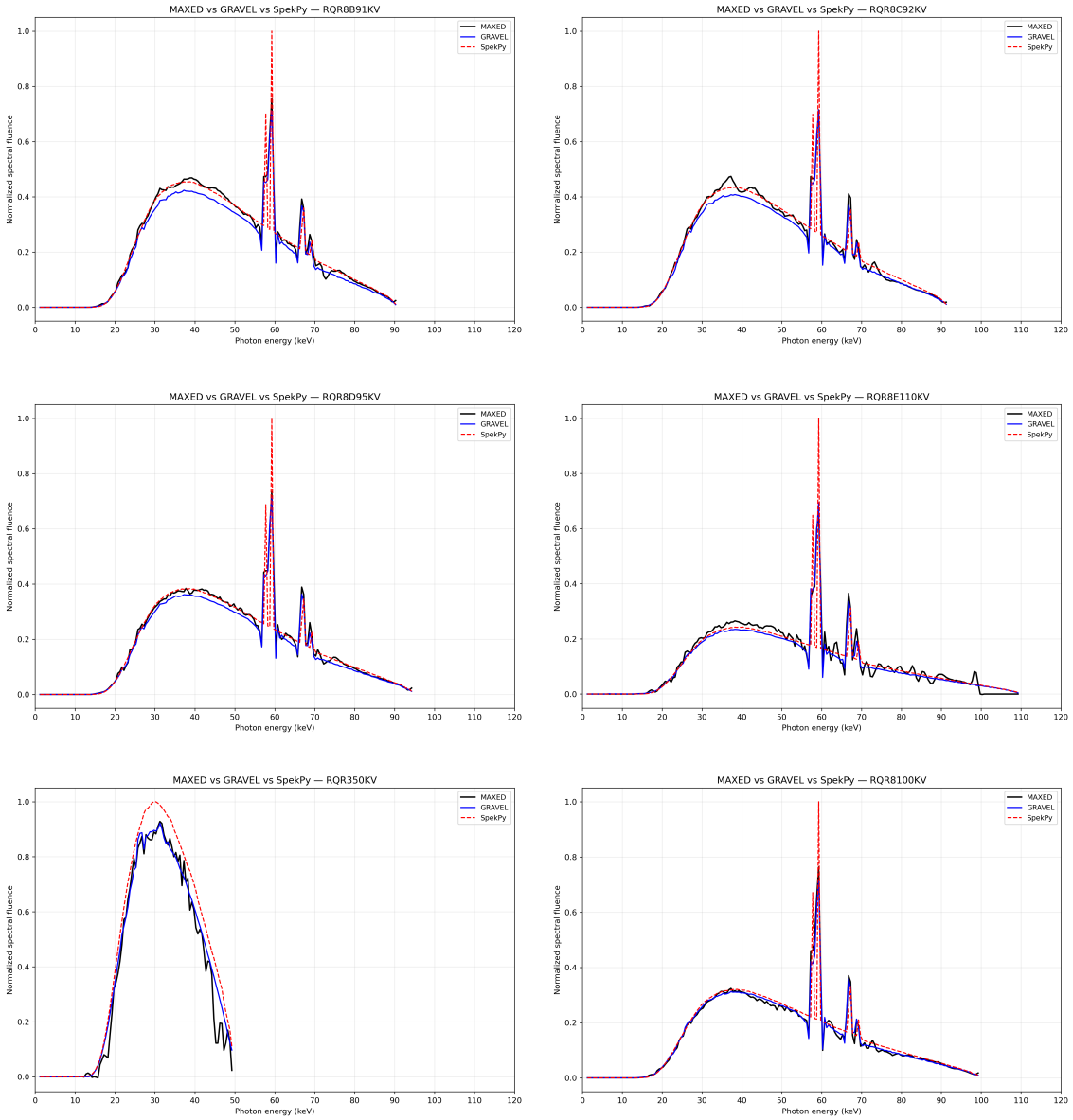

Figure I.4: Comparison of unfolded spectra obtained with MAXED and GRAVEL against SpekPy reference spectra.

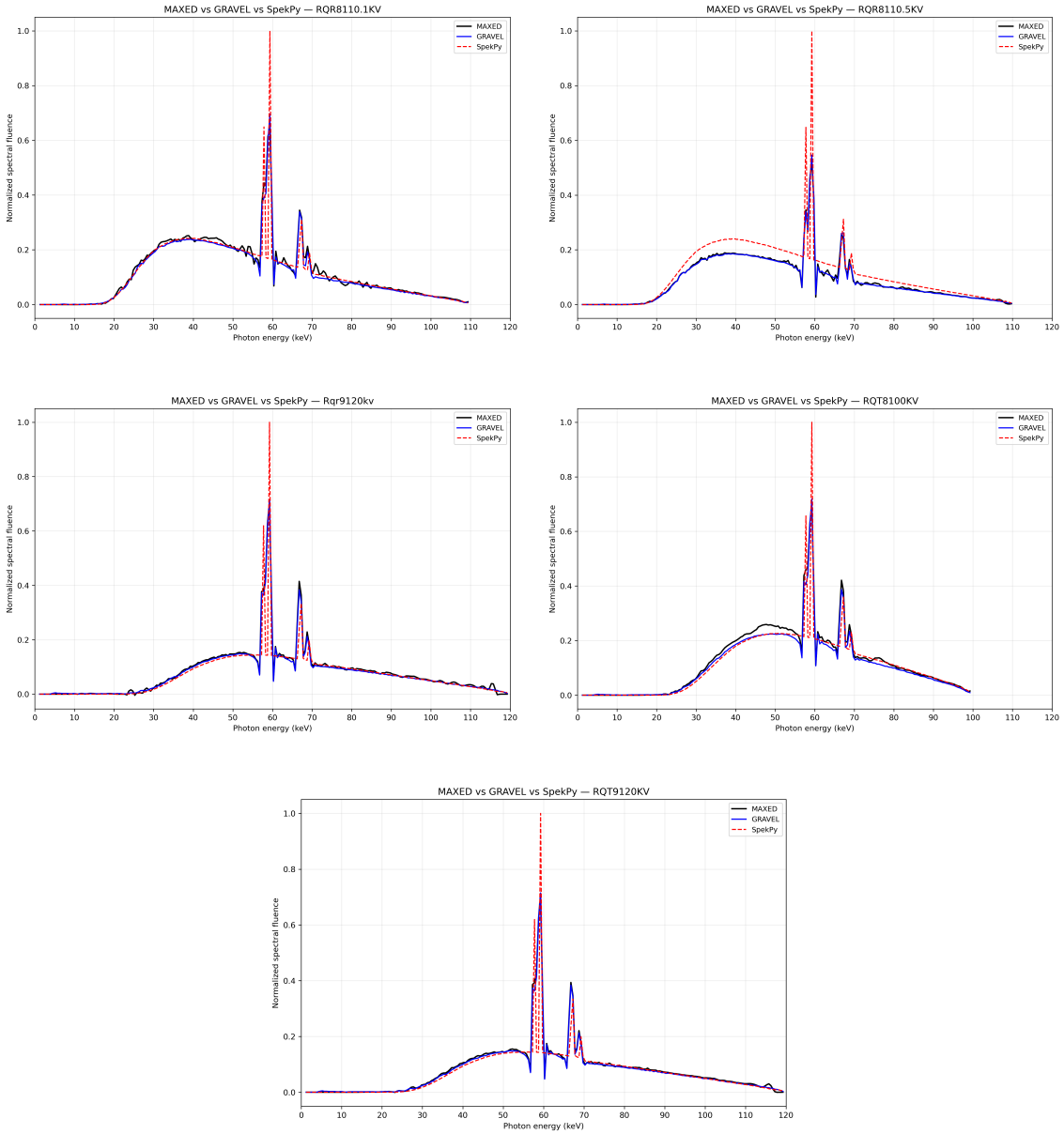

Figure I.5: Comparison of unfolded spectra obtained with MAXED and GRAVEL against SpekPy reference spectra for the remaining ISO 4037 beam qualities.